

# Pump Free Microwave-Optical Quantum Transduction

Fangxin Li,<sup>1,\*</sup> Jaesung Heo,<sup>2,†</sup> Zhaoyou Wang,<sup>2</sup> Andrew P. Higginbotham,<sup>1,3</sup> Alexander A. High,<sup>2</sup> and Liang Jiang<sup>2,‡</sup>

<sup>1</sup>*Department of Physics, University of Chicago, Chicago, IL 60637, USA*

<sup>2</sup>*Pritzker School of Molecular Engineering, University of Chicago, Chicago, Illinois 60637, USA*

<sup>3</sup>*James Franck Institute, University of Chicago, Chicago, IL 60637, USA*

(Dated: December 5, 2025)

Distributed quantum computing involves superconducting computation nodes operating at microwave frequencies, which are connected by long-distance transmission lines that transmit photons at optical frequencies. Quantum transduction, which coherently converts between microwave and optical (M-O) photons, is a critical component of such an architecture. Current approaches are hindered by the unavoidable problem of device heating due to the optical pump. In this work, we propose a pump-free scheme based on color centers that generates time-bin encoded M-O Bell pairs. Our scheme first creates spin-photon entanglement and then converts the spin state into a time-bin-encoded microwave photon using a strongly coupled Purcell-enhanced resonator. In our protocol, the microwave retrieval is heralded by detecting the microwave signal with a three-level transmon. We have analyzed the resulting Bell state fidelity and generation probability of this protocol. Our simulation shows that by combining a state-of-the-art spin-optical interface with our proposed strongly-coupled spin-microwave design, the pump-free scheme can generate M-O Bell pairs at a heralding rate exceeding one kilohertz with near-unity fidelity, which establishes the scheme as a promising source for M-O Bell pairs.

**Introduction**—The vision of a quantum internet promises secure communication, distributed quantum computing, and enhanced sensing by interconnecting heterogeneous quantum systems over long distances [1]. To interface quantum devices working at disparate frequency regimes, a key enabling technology is quantum transduction—the coherent conversion of quantum states between optical and microwave frequency domains [1–5]. Many platforms have pursued this goal using nonlinear interactions activated by strong pump fields [4–24]. However, the strong optical pumps required for these interactions are practically challenging with the cryogenic environments crucial for superconducting microwave devices. Many current transduction protocols suffer from pump-induced heating, which degrades superconductivity, adds thermal noise, and reduces conversion fidelity [4, 5, 9, 12, 15–17, 21, 23–30]. Therefore, a transduction protocol that does not rely on an optical pump is another promising route toward high-fidelity quantum transduction devices, which will serve as robust components in the quantum interconnect.

Such a pump-free protocol can be realized using diamond color centers [31–33], which possess both optical and microwave spin transitions and therefore provide a natural interface between optical and microwave photons. Recent experiments have demonstrated high-cooperativity coupling between single color centers and nanophotonic cavities, together with coherent microwave control of their spin levels [34–36]. This has enabled entanglement between time-bin encoded optical photons and a spin transition with microwave-range separation,

a key ingredient for quantum networks, distributed computing, and blind quantum computing [37–39].

To generate M-O entanglement, the microwave excitation stored in the spin must be retrieved via a Purcell-enhanced resonator before decoherence. While diamond color centers are compatible with superconducting devices from a materials perspective—requiring zero or only small DC magnetic fields for microwave spin-level splitting, integrating them with the optical cavity introduces a key constraint: the optical cavity cannot be placed in close proximity to the resonator’s metal, where optical absorption and scattering losses would degrade perfor-

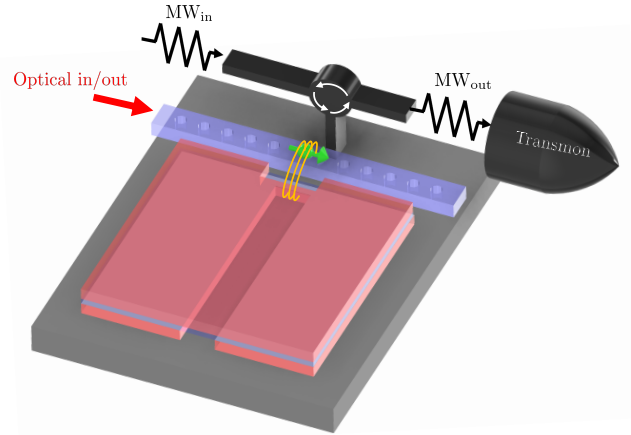


FIG. 1. Schematic of the hybrid microwave-resonator-optical-cavity device for pump-free quantum transduction. The microwave resonator incorporates a diamond-sandwiched parallel-plate capacitor that enables strong coupling to a spin qubit in a one-dimensional photonic crystal cavity, thereby facilitating heralded generation of microwave-optical Bell pairs.

\* fangxinli@uchicago.edu; Equal contribution.

† jheo@uchicago.edu; Equal contribution.

‡ liangjiang@uchicago.edu

mance [40]. Consequently, the optical cavity must be kept sufficiently far from the metal, demanding a large microwave coupling rate at separations of several hundred nanometers. In this regime, the strongest reported single-spin coupling is a few kilohertz, achieved using  $\text{Er}^{3+}$  ions [41]. The challenge is even greater for diamond color centers, which are limited by a smaller gyromagnetic ratio. We propose to overcome these challenges with a new resonator design, shown in Fig. 1, that utilizes a parallel plate capacitor structure. This architecture enhances the single-spin microwave coupling rate by an order of magnitude while remaining compatible with a high-quality optical interface. This enables strong microwave-optical hybrid coupling for diamond defect centers.

With this hybrid device, we propose a pump-free quantum transduction scheme based on a single color center in diamond, capable of generating time-bin encoded M-O Bell pairs. The protocol unfolds in two steps. First, we leverage a well-established spin-photon entanglement protocol to entangle an itinerant optical photon with the spin states of the color center [35, 36, 42, 43]. Second, the entangled spin state decays through a Purcell-enhanced microwave resonator, converting the spin state into a time-bin-encoded microwave photon. This microwave photon is captured by a three-level transmon [44–48], heralding the successful creation of an M-O Bell pair. To establish the feasibility of this protocol, we use the nitrogen-vacancy center ( $\text{NV}^-$ ) [49–51], as well as the tin-vacancy center with strong nuclear hyperfine coupling ( $^{117}\text{SnV}^-$ ) [52] as examples in our analysis. With the proposed architecture, which achieves a microwave single-photon coupling rate  $g_m/2\pi$  of a few kilohertz with diamond color centers, our pump-free transduction scheme can generate M-O Bell pairs at intrinsic heralding rates in the kilohertz range, all while maintaining near-unit fidelity.

*Entangling protocol*— We first describe the pump-free scheme in general, independent of the specific color center used. Then, we demonstrate the performance of our scheme using the nitrogen-vacancy center ( $\text{NV}^-$ ), as well as the tin-vacancy center with strong nuclear hyperfine coupling ( $^{117}\text{SnV}^-$ ). The two color defects exhibit well-resolved optical transitions and microwave controllability, and possesses the level structure required for our scheme as shown in Fig. 2(a) [52]. In Appendix E, we discuss the application of our scheme to other color centers.

Our entanglement generation protocol is realized in two steps. First, spin-photon entanglement is generated by spin-dependent optical reflectivity, a well-established, high-fidelity protocol for diamond color centers in photonic cavities [35, 36, 42, 43]. Different spin states in the ground state manifold couple to optical excitation with different transition frequencies, such as  $f_0$  and  $f_1$  illustrated in Fig. 2(a), giving rise to distinct optical reflectivities. We adopt a scheme where the  $|0\rangle$  state is highly reflective and the  $|1\rangle$  state is non-reflective. The system

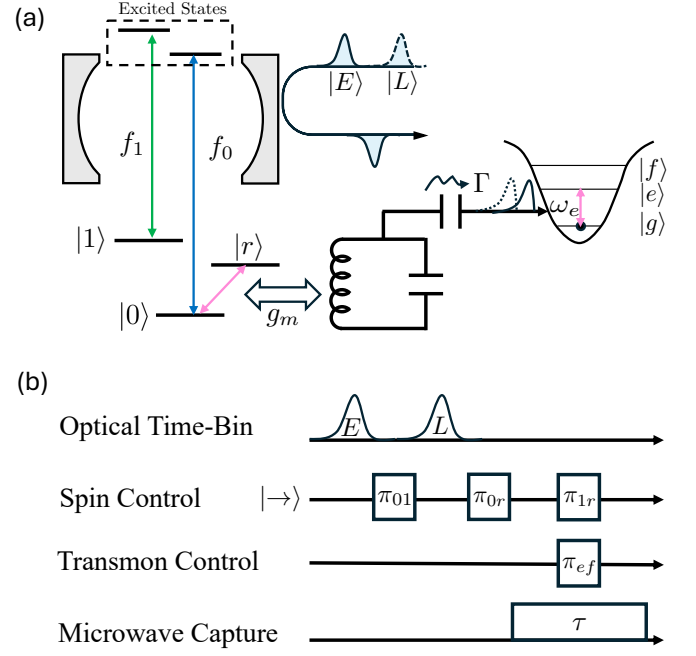


FIG. 2. (a) Illustration of the protocol with level schemes for the color center and a superconducting transmon qubit. The color center couples to an optical cavity and a microwave resonator. (b) Operation scheme in time sequence for spin-photon entanglement and microwave retrieval, where  $\pi_{0r}$  represents a  $\pi$ -rotation in the  $|0\rangle, |r\rangle$  subspace of the three-level system.

is initialized in a product state: the incoming photon is prepared in a superposition of early ( $|E\rangle$ ) and late ( $|L\rangle$ ) time-bins, and the spin is prepared in the superposition  $|\rightarrow\rangle = (|0\rangle + |1\rangle)/\sqrt{2}$ . As shown in Fig. 2(b), a  $\pi$ -pulse applied to the spin between the two time-bins entangles the reflected photon with the spin, creating the final spin-photon Bell state:  $|\Phi\rangle_{\text{Photon,Spin}} = (|E\rangle|1\rangle + |L\rangle|0\rangle)/\sqrt{2}$ , with a 0.5 probability. The protocol can achieve near-unit Bell state fidelity with the success probability limited by the system cooperativity. A series of experiments has demonstrated the protocol [35–39], and the best-achievable Bell state fidelity has been shown to exceed 0.97 [39].

Next, we retrieve the spin state using a superconducting microwave resonator. The resulting microwave signal is then captured by a three-level transmon to herald successful Bell pair creation. We model the coupling between the color center and a microwave resonator as the Jaynes-Cummings Hamiltonian:  $H_{\text{int}} = \hbar g_m (\hat{a}\sigma_+ + \hat{a}^\dagger\sigma_-)$ , where  $g_m$  is the single-photon microwave coupling,  $\hat{a}$  represents the microwave resonator mode, and  $\sigma_+ = |r\rangle\langle 0|$  and  $\sigma_- = |0\rangle\langle r|$  are operators associated with the readout transition shown in Fig. 2(a). The spin transition is resonant with the microwave resonator mode, which has an external coupling rate  $\kappa_m$ . Spin state retrieval is in the Purcell regime, where the resonator-enhanced spin relaxation is the dominant process, with a rate  $\Gamma = 4g_m^2/\kappa_m$  for

$g_m \lesssim \kappa_m$ . By further tuning the resonator external coupling rate to match the spin coupling rate, the optimal emission rate can be  $\Gamma \sim g_m$ .

To convert a spin qubit state  $\alpha|0\rangle + \beta|1\rangle$  into a microwave time-bin state, we work in the Purcell-enhanced regime by tuning the resonator in resonance with the readout level and suppressing the decay of the off-resonant  $|1\rangle$  state. We create two time-bins by sequentially transferring the population from the  $|0\rangle$  and the  $|1\rangle$  states to the readout level  $|r\rangle$  using microwave control pulses, as shown in Fig. 2(b), and allowing the level  $|r\rangle$  to decay through the cavity. The microwave control pulses are fast, high-fidelity operations, and spin relaxation during control is negligible, as demonstrated in [52, 53].

To herald successful entanglement events, the time-bin photons are then captured by a three-level transmon [44–48]. As shown in Fig. 2(a), we tune the  $g$ - $e$  transition of the transmon to be in resonance with the Purcell-enhanced emission from the spin excitation to efficiently absorb the emitted microwave photons. To map the time-bin state onto a transmon state, the photon from the first time-bin can be shelved in the  $|f\rangle$  level of the transmon, thereby freeing the  $g$ - $e$  transition to capture the photon from the second time-bin, as shown in Fig. 2(b). If the transfer is successful and lossless, the two time-bin components are mapped to the  $|e\rangle, |f\rangle$  subspace; otherwise, loss results in the transmon remaining in the  $|g\rangle$  state, which enables error detection. Therefore, successful entanglement generation events will create the optical-transmon Bell state  $|\Psi\rangle_{\text{Photon, Transmon}} = (|E\rangle|e\rangle + |L\rangle|f\rangle)/\sqrt{2}$ .

The performance of the above microwave heralding scheme depends critically on the Purcell-enhanced microwave photon emission rate  $\Gamma$ , which should exceed the decoherence and dissipation rates of the system. To understand this competition, we analyze the probability of microwave retrieval and Bell state fidelity as functions of time  $\tau$ . As an initial estimate, we model the heralding probability as the probability of a microwave photon leaving the cavity over a time  $\tau$ :

$$P_{\text{mw}} = 1 - e^{-\Gamma\tau}. \quad (1)$$

The dominant infidelity contributions over this same window arise from spin dephasing described by the color center's  $T_{2,s}$  and transmon relaxation  $T_{1,t}$ . The dephasing process occurs throughout the time window  $\tau$ , while relaxation of the transmon occurs after the shelving. The error process can be modeled by a dephasing channel combined with an amplitude damping channel (see Appendix D). The microwave retrieval process has entanglement fidelity:

$$F_{\text{mw}} = \frac{1}{4}(1 + e^{-\tau/T_{1,t}} + 2e^{-\tau/2T_{1,t}}e^{-\tau/T_{2,s}}). \quad (2)$$

For the spin-optical protocol which favors high fidelity, the probability for creating a unit-fidelity spin-photon Bell pair is upper bounded by  $P_{\text{opt}} = 0.5C^2/(C+1)^2$  (see

Appendix C), where  $C$  is the system cooperativity defined by  $C = \frac{g_o^2}{\kappa_o\gamma_o}$ . The prefactor 0.5 is due to the non-reflective spin state, which discards photons half of the time. Here,  $g_o$  is the coupling between the color center and the optical cavity;  $\kappa_o$  is the loss rate of the optical cavity, and  $\gamma_o$  is the optical free-space decay rate of the tin-vacancy. Taking into account both the spin-optical entanglement and the spin-microwave retrieval processes, the overall performance of our scheme is given by the Bell state creation fidelity  $\mathcal{F} = F_{\text{mw}}$  and the probability  $\mathcal{P} = P_{\text{opt}}P_{\text{mw}}$ . To efficiently generate high-fidelity M-O Bell pairs using this scheme, we are thus required to design a high-cooperativity spin-optical interface together with a strongly coupled microwave-resonator system that releases microwave photons before the system decoheres.

*Microwave Strong Coupling Design*—We present a new microwave resonator design that achieves a strong coupling rate  $g_m$  even at a distance where the optical cavity maintains high cooperativity  $C$  despite metal-induced loss.

To maximize the coupling between the spin and the microwave resonator, a large magnetic zero-point fluctuation at the spin location is required. This field originates from the zero-point current fluctuations  $\delta I$ . For a lumped-element LC resonator with resonance frequency  $\omega_R = 1/\sqrt{LC}$ ,

$$\delta I = \omega_R \sqrt{\frac{\hbar}{2Z}}, \quad (3)$$

where  $Z = \sqrt{L/C}$  is the characteristic impedance of the resonator [56]. Because the resonance frequency is fixed by the spin transition, the design goal is to keep  $\omega_R$  constant while minimizing  $Z$ .

The central element of our design is the use of a parallel-plate capacitor (Fig. 1). Previous spin-resonator coupling implementations have employed an interdigitated capacitor (IDC), where the capacitance originates from the electric field between interleaved fingers [41, 56–58]. Increasing the capacitance in this geometry requires many long fingers, which enlarge the device area and introduce significant stray inductance [41, 57, 58], thus limiting impedance reduction. In contrast, the parallel-plate configuration provides orders of magnitude larger capacitance with minimal stray inductance, yielding a characteristic impedance up to three orders of magnitude lower than that of previously reported microwave resonators [41, 57, 58].

The details of the resonator design are shown in Fig. 3(a). The microwave resonator consists of a three-level structure that effectively forms a parallel LC circuit. The bottom layer (level 1) comprises two large superconducting (SC) pads connected by a narrow inductive wire. The entire region is covered by a 100 nm thick single-crystal diamond layer (level 2) [59, 60]. A large superconducting pad (level 3) covers the entire area except for the wire region, thereby suppressing image-current formation without significantly reducing the capacitance. Together,

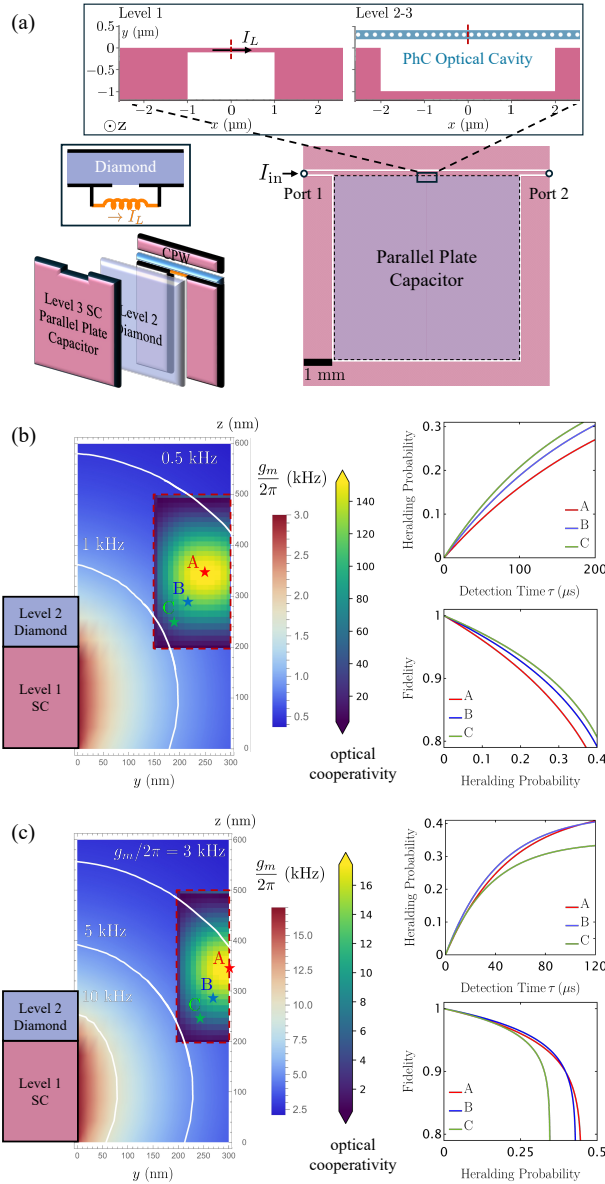


FIG. 3. (a) Hybrid optical-cavity-microwave-resonator design demonstrating the feasibility of the pump-free quantum transduction protocol. The microwave resonator is modeled as a parallel LC circuit, with a coplanar waveguide (CPW) placed above it for signal input and readout. The resonator shown here is designed for the  $^{117}\text{SnV}^-$  center. A one-dimensional photonic crystal cavity is positioned near the inductive-wire region of the resonator to achieve both strong microwave coupling and high optical cooperativity. (b,c) Simulation results at the center of the cavity (red dashed line in (a)) and the corresponding figures of merit for (b) the  $^{117}\text{SnV}^-$  center and (c) the  $\text{NV}^-$  center. For the fidelity calculation, we use  $T_{1,t} = 1$  ms and  $T_{2,s} = 2.5$  ms for the  $^{117}\text{SnV}^-$  center, and  $T_{2,s} = 1$  ms for the  $\text{NV}^-$  center [52, 54, 55].

these layers form a parallel-plate capacitor that realizes the capacitive element of the LC circuit. The zero-point magnetic field fluctuation arises from the zero-point current fluctuations in the inductive wire (level 1). The tar-

	$\text{NV}^-$ [50]	$^{117}\text{SnV}^-$ [52]
Radiative Lifetime $\tau_{\text{rad}}$	13 ns	6 ns
Debye-Waller Factor $\xi$	0.03	0.6
Electric Dipole	$5.1 D$	$7.3 D$
DC Magnetic Field $\vec{B}$	0.1-1 mT	0
Engineered Strain $\alpha$	0	900 GHz
MW qubit frequency (GHz)	2.9	0.6
Magnetic Dipole	$\gamma_e/\sqrt{2}$	$\frac{\gamma_e}{2\sqrt{2}} \frac{\alpha}{\sqrt{\alpha^2 + \lambda^2}}$
Characteristic Impedance $Z$	$0.12 \Omega$	$0.027 \Omega$
Zero-Point Current Fluctuations $\delta I$	377 nA	178 nA
Capacitor Size ( $\text{mm}^2$ )	$0.95 \times 1.9$	$4.2 \times 8.5$

TABLE I. Comparison between different candidate color centers.  $\gamma_e$  is the gyromagnetic ratio of the electron. The magnetic dipole of the tin-vacancy center depends on the strain  $\alpha$  in the system, and the spin-orbit coupling  $\lambda = 830$  GHz (see Appendix E). Here,  $D = 3.34 \times 10^{-30} \text{ C} \cdot \text{m}$ . Color center parameters are used for calculating the optical cooperativity and spin microwave coupling strength.

get diamond defect center is embedded in the photonic crystal cavity positioned near the wire section of the resonator to ensure a large coupling rate  $g_m$ .

To send and read out microwave signals, a coplanar waveguide (CPW) is used with ports labeled 1 and 2. To evaluate the zero-point current fluctuations at the inductive wire  $I_L$  in response to an input signal on the CPW, we analyzed the current-current susceptibility defined as  $\chi_{II} = I_L/I_+$ , where  $I_+$  is the current incident at port 1. The zero-point fluctuations are then obtained as (see Appendix A 2 for details)

$$\delta I^2 = \frac{\hbar \omega_R}{2Z_0} \int_{-\infty}^{\infty} 2 |\chi_{II}(\omega)|^2 \frac{d\omega}{2\pi}, \quad (4)$$

where  $Z_0 = 50 \Omega$  is the characteristic impedance of CPW.

To demonstrate the feasibility of our protocol, we consider the  $\text{NV}^-$  and the  $^{117}\text{SnV}^-$  center as examples. The properties of the two color centers are compared in Table I and elaborated in Appendix E. A key operational difference lies in the magnetic field requirement. The  $\text{NV}^-$  requires a small DC magnetic field (on the order of milli-Tesla) to lift its ground-state level degeneracy. In contrast, the  $^{117}\text{SnV}^-$  allows for a zero-field protocol, as its ground state is already split by strain engineering and strong hyperfine interaction [52]. Optically, the  $^{117}\text{SnV}^-$  is much more efficient than the  $\text{NV}^-$ , which ensures a high spin-photon entanglement probability. This advantage in the  $^{117}\text{SnV}^-$ , however, is offset by a trade-off in the microwave domain. It has a reduced magnetic dipole moment compared to the  $\text{NV}^-$ , which results in lower microwave retrieval efficiency.

To understand the performance of our scheme, we simulate the device architecture designed for the color centers described in the previous paragraph. The inductive wire dominates the total inductance of the resonator, yielding  $L = 6.7$  pH, which is two orders of magnitude smaller than the inductance of resonators employing an IDC design. The capacitor area is adjusted to match



the microwave transition frequency of each color center, leading to different characteristic impedances and corresponding zero-point currents, as summarized in Table I. The resulting simulated coupling rate  $g_m$  for the  $^{117}\text{SnV}^-$  and  $\text{NV}^-$  centers are shown in Figs. 3(b) and 3(c), respectively. The insets display the corresponding optical cooperativity where the cavity design follows Ref. [61]. Due to its larger magnetic dipole moment, the  $\text{NV}^-$  center achieves a microwave coupling rate  $g_m$  that is 5.64 times stronger than that of the  $^{117}\text{SnV}^-$  center. However, its small Debye-Waller factor suppresses the optical cooperativity, which is 18 times lower than that of the  $^{117}\text{SnV}^-$  center, assuming the same optical-cavity-inductive-wire separation. These trade-offs are directly reflected in the figures of merit for the selected spin positions (marked by stars in the plots). For the  $^{117}\text{SnV}^-$  ( $\text{NV}^-$ ) center, a fidelity of 90% is achieved with a detection time of 153  $\mu\text{s}$  (107  $\mu\text{s}$ ), corresponding to a maximum heralding probability of 27.7 % (39.6 %). (See Supplementary Information.)

Experimentally, the total runtime is determined by the heralding rate, which depends on the protocol's success probability and cycle duration. Using simulated results, we calculate the intrinsic heralding rate of our scheme, which excludes decreases in the heralding rate due to external collection efficiencies, such as optical fiber coupling, signal transmission losses, and detector efficiency.

The intrinsic heralding rate  $R_{\text{herald}}$  can be estimated as:  $R_{\text{herald}} = \mathcal{P}/T_r$ , where  $\mathcal{P}$  is the success probability of our scheme and  $T_r$  is the time taken for each round of Bell pair generation.  $T_r$  is mainly limited by the detection time  $\tau$ , but we also take into account the reset time and gate time  $T_{\text{reset}}$ . The intrinsic heralding rate, therefore, can be expressed as

$$R_{\text{herald}} = 0.5 \cdot \frac{C^2}{(1+C)^2} \cdot \frac{(1 - e^{-\Gamma\tau})}{\tau + T_{\text{reset}}}. \quad (5)$$

To maximize the heralding probability, we optimized the detection time  $\tau$ . Our simulations reveal that the optimal regime employs a short, truncated detection window rather than capturing the complete signal in each round (see Appendix F). This truncated detection approach also ensures the high fidelity of the heralded Bell pairs.

Using the simulated parameters listed in Appendix. F, the optimization yields superior intrinsic performance for the  $\text{NV}^-$ : an intrinsic heralding rate of 5.6 kHz and a fidelity of 0.97, compared to 2.0 kHz and 0.96 for the  $^{117}\text{SnV}^-$ . Notably, the  $\text{NV}^-$  slightly outperforms the  $^{117}\text{SnV}^-$  in both metrics, despite having a smaller cooperativity. This advantage is attributed to the  $\text{NV}^-$ 's larger magnetic dipole moment. Consequently, the  $\text{NV}^-$  presents a more efficient and high-fidelity pathway for Bell pair generation, provided a small magnetic field is compatible with the experimental design. The  $^{117}\text{SnV}^-$ , however, remains a strong candidate for protocols requiring strictly zero-field operation.

*Discussion and Summary*—Our scheme considers a single-spin system, which limits the achievable coupling rates. A possible extension is to implement the protocol using a spin ensemble of  $N$  emitters, which would acquire a  $\sqrt{N}$  boost in both the optical and microwave coupling at the cost of facing collective dephasing and inhomogeneous broadening.

For implementing the parallel-plate capacitor design in experiment, a clean interface between diamond and a superconducting material is essential. In this direction, crystalline dielectrics such as hBN have been shown to form high-quality interfaces with superconductors, supporting low loss tangents and high internal quality factors [62]. Single-crystalline diamond thin films can be directly bonded to a wide range of materials and complex structures containing oxide layers [59, 60], suggesting potential for low-loss diamond-superconductor interfaces. Niobium (Nb) is a promising superconducting material due to its native oxide layer and high internal quality factor [63]. To operate in the good-cavity regime, the total quality factor must exceed  $10^6$ , making it crucial to achieve a high internal quality factor.

In summary, we propose a pump-free scheme for generating M-O Bell pairs based on a single color center in diamond with both strong optical and microwave transitions. To establish the protocol's feasibility, we have designed a strongly-coupled microwave resonator that is compatible with a high-cooperativity optical cavity. The resulting hybrid device achieves a high intrinsic heralding rate exceeding one kilohertz while maintaining the high fidelity essential for quantum information processing across hybrid physical platforms.

## ACKNOWLEDGMENTS

We acknowledge helpful discussions with Benjamin Pingault, Xingyu Gao, Yang Shen, and Christopher Wang. We acknowledge support from the ARO(W911NF-23-1-0077), ARO MURI (W911NF-21-1-0325), AFOSR MURI (FA9550-19-1-0399, FA9550-21-1-0209, FA9550-23-1-0338), DARPA (HR0011-24-9-0359, HR0011-24-9-0361), NSF (OMA-1936118, ERC-1941583, OMA-2137642, OSI-2326767, CCF-2312755), Packard Foundation (2020-71479), and the Marshall and Arlene Bennett Family Research Program. This material is based upon work supported by the U.S. Department of Energy, Office of Science, National Quantum Information Science Research Centers and Advanced Scientific Computing Research (ASCR) program under contract number DE-AC02-06CH11357 as part of the InterQnet quantum networking project. This work was completed with resources provided by the University of Chicago's Research Computing Center. We acknowledge support from the Quantum Leap Challenge Institute for Hybrid Quantum Architectures and Networks (HQAN) (NSF OMA-2016136). We acknowledge help from the Sonnet Software Technical Support.

- 
- [1] H. J. Kimble, The quantum internet, *Nature* **453**, 1023 (2008).
- [2] J. I. Cirac, P. Zoller, H. J. Kimble, and H. Mabuchi, Quantum state transfer and entanglement distribution among distant nodes in a quantum network, *Phys. Rev. Lett.* **78**, 3221 (1997).
- [3] J. Bochmann, A. Vainsencher, D. D. Awschalom, and A. N. Cleland, Nanomechanical coupling between microwave and optical photons, *Nature Physics* **9**, 712 (2013).
- [4] N. Lauk, N. Sinclair, S. Barzanjeh, J. P. Covey, M. Saffman, M. Spiropulu, and C. Simon, Perspectives on quantum transduction, *Quantum Science and Technology* **5**, 020501 (2020).
- [5] X. Han, W. Fu, C.-L. Zou, L. Jiang, and H. X. Tang, Microwave-optical quantum frequency conversion, *Optica* **8**, 1050 (2021).
- [6] M. Hafezi, Z. Kim, S. L. Rolston, L. A. Orozco, B. L. Lev, and J. M. Taylor, Atomic interface between microwave and optical photons, *Phys. Rev. A* **85**, 020302 (2012).
- [7] R. Hisatomi, A. Osada, Y. Tabuchi, T. Ishikawa, A. Noguchi, R. Yamazaki, K. Usami, and Y. Nakamura, Bidirectional conversion between microwave and light via ferromagnetic magnons, *Phys. Rev. B* **93**, 174427 (2016).
- [8] B. T. Gard, K. Jacobs, R. McDermott, and M. Saffman, Microwave-to-optical frequency conversion using a cesium atom coupled to a superconducting resonator, *Phys. Rev. A* **96**, 013833 (2017).
- [9] A. P. Higginbotham, P. S. Burns, M. D. Urmey, R. W. Peterson, N. S. Kampel, B. M. Brubaker, G. Smith, K. W. Lehnert, and C. A. Regal, Harnessing electro-optic correlations in an efficient mechanical converter, *Nature Physics* **14**, 1038 (2018).
- [10] L. Fan, C.-L. Zou, R. Cheng, X. Guo, X. Han, Z. Gong, S. Wang, and H. X. Tang, Superconducting cavity electro-optics: A platform for coherent photon conversion between superconducting and photonic circuits, *Science Advances* **4**, eaar4994 (2018).
- [11] T. Vogt, C. Gross, J. Han, S. B. Pal, M. Lam, M. Kiffner, and W. Li, Efficient microwave-to-optical conversion using rydberg atoms, *Phys. Rev. A* **99**, 023832 (2019).
- [12] A. Rueda, W. Hease, S. Barzanjeh, and J. M. Fink, Electro-optic entanglement source for microwave to telecom quantum state transfer, *npj Quantum Information* **5**, 108 (2019).
- [13] C. Zhong, Z. Wang, C. Zou, M. Zhang, X. Han, W. Fu, M. Xu, S. Shankar, M. H. Devoret, H. X. Tang, and L. Jiang, Proposal for heralded generation and detection of entangled microwave-optical-photon pairs, *Phys. Rev. Lett.* **124**, 010511 (2020).
- [14] W. Jiang, C. J. Sarabalis, Y. D. Dahmani, R. N. Patel, F. M. Mayor, T. P. McKenna, R. Van Laer, and A. H. Safavi-Naeini, Efficient bidirectional piezo-optomechanical transduction between microwave and optical frequency, *Nature Communications* **11**, 1166 (2020).
- [15] M. Mirhosseini, A. Sipahigil, M. Kalaei, and O. Painter, Superconducting qubit to optical photon transduction, *Nature* **588**, 599 (2020).
- [16] J. Holzgrafe, N. Sinclair, D. Zhu, A. Shams-Ansari, M. Colangelo, Y. Hu, M. Zhang, K. K. Berggren, and M. Lončar, Cavity electro-optics in thin-film lithium niobate for efficient microwave-to-optical transduction, *Optica* **7**, 1714 (2020).
- [17] S. Krastanov, H. Raniwala, J. Holzgrafe, K. Jacobs, M. Lončar, M. J. Reagor, and D. R. Englund, Optically heralded entanglement of superconducting systems in quantum networks, *Phys. Rev. Lett.* **127**, 040503 (2021).
- [18] J. Wu, C. Cui, L. Fan, and Q. Zhuang, Deterministic microwave-optical transduction based on quantum teleportation, *Phys. Rev. Appl.* **16**, 064044 (2021).
- [19] C. Zhong, X. Han, and L. Jiang, Microwave and optical entanglement for quantum transduction with electro-optomechanics, *Phys. Rev. Appl.* **18**, 054061 (2022).
- [20] R. Sahu, L. Qiu, W. Hease, G. Arnold, Y. Minoguchi, P. Rabl, and J. M. Fink, Entangling microwaves with light, *Science* **380**, 718 (2023).
- [21] J. Rochman, T. Xie, J. G. Bartholomew, K. C. Schwab, and A. Faraon, Microwave-to-optical transduction with erbium ions coupled to planar photonic and superconducting resonators, *Nature Communications* **14**, 1153 (2023).
- [22] S. Meesala, S. Wood, D. Lake, P. Chiappina, C. Zhong, A. D. Beyer, M. D. Shaw, L. Jiang, and O. Painter, Non-classical microwave-optical photon pair generation with a chip-scale transducer, *Nature Physics* **20**, 871–877 (2024).
- [23] S. Meesala, D. Lake, S. Wood, P. Chiappina, C. Zhong, A. D. Beyer, M. D. Shaw, L. Jiang, and O. Painter, Quantum entanglement between optical and microwave photonic qubits, *Phys. Rev. X* **14**, 031055 (2024).
- [24] T. Xie, R. Fukumori, J. Li, and A. Faraon, Scalable microwave-to-optical transducers at the single-photon level with spins, *Nature Physics* **21**, 931 (2025).
- [25] S. M. Meenehan, J. D. Cohen, S. Gröblacher, J. T. Hill, A. H. Safavi-Naeini, M. Aspelmeyer, and O. Painter, Silicon optomechanical crystal resonator at millikelvin temperatures, *Phys. Rev. A* **90**, 011803 (2014).
- [26] S. M. Meenehan, J. D. Cohen, G. S. MacCabe, F. Marsili, M. D. Shaw, and O. Painter, Pulsed excitation dynamics of an optomechanical crystal resonator near its quantum ground state of motion, *Phys. Rev. X* **5**, 041002 (2015).
- [27] G. S. MacCabe, H. Ren, J. Luo, J. D. Cohen, H. Zhou, A. Sipahigil, M. Mirhosseini, and O. Painter, Nanoacoustic resonator with ultralong phonon lifetime, *Science* **370**, 840 (2020).
- [28] H. Ren, M. H. Matheny, G. S. MacCabe, J. Luo, H. Pfeifer, M. Mirhosseini, and O. Painter, Two-dimensional optomechanical crystal cavity with high quantum cooperativity, *Nature Communications* **11**, 3373 (2020).
- [29] C. Zhong, F. Li, S. Meesala, S. Wood, D. Lake, O. Painter, and L. Jiang, Microwave-optical entanglement from pulse-pumped electro-optomechanics, *Phys. Rev. Appl.* **22**, 064047 (2024).
- [30] G. Arnold, T. Werner, R. Sahu, L. N. Kapoor, L. Qiu, and J. M. Fink, All-optical superconducting qubit readout, *Nature Physics* **21**, 393 (2025).
- [31] A. Tchegotareva, S. L. N. Hermans, P. C. Humphreys, D. Voigt, P. J. Harmsma, L. K. Cheng, A. L. Verlaan, N. Dijkhuizen, W. de Jong, A. Dréau, and R. Hanson, Entanglement between a diamond spin qubit and a photonic time-bin qubit at telecom wavelength, *Phys. Rev.*

- Lett.* **123**, 063601 (2019).
- [32] E. I. Rosenthal, C. P. Anderson, H. C. Kleidermacher, A. J. Stein, H. Lee, J. Grzesik, G. Scuri, A. E. Rugar, D. Riedel, S. Aghaeimeibodi, G. H. Ahn, K. Van Gasse, and J. Vučković, Microwave spin control of a tin-vacancy qubit in diamond, *Phys. Rev. X* **13**, 031022 (2023).
  - [33] X. Guo, A. M. Stramma, Z. Li, W. G. Roth, B. Huang, Y. Jin, R. A. Parker, J. A. Martínez, N. Shofer, C. P. Michaels, C. P. Purser, M. H. Appel, E. M. Alexeev, T. Liu, A. C. Ferrari, D. D. Awschalom, N. Delegan, B. Pingault, G. Galli, F. J. Heremans, M. Atatüre, and A. A. High, Microwave-based quantum control and coherence protection of tin-vacancy spin qubits in a strain-tuned diamond-membrane heterostructure, *Physical Review X* **13**, 10.1103/PhysRevX.13.041037 (2023).
  - [34] A. Sipahigil, R. E. Evans, D. D. Sukachev, M. J. Burek, J. Borregaard, M. K. Bhaskar, C. T. Nguyen, J. L. Pacheco, H. A. Atikian, C. Meuwly, R. M. Camacho, F. Jelezko, E. Bielejec, H. Park, M. Lončar, and M. D. Lukin, An integrated diamond nanophotonics platform for quantum-optical networks, *Science* **354**, 847 (2016).
  - [35] C. T. Nguyen, D. D. Sukachev, M. K. Bhaskar, B. Machielse, D. S. Levonian, E. N. Knall, P. Stroganov, C. Chia, M. J. Burek, R. Riedinger, H. Park, M. Lončar, and M. D. Lukin, An integrated nanophotonic quantum register based on silicon-vacancy spins in diamond, *Phys. Rev. B* **100**, 165428 (2019).
  - [36] C. T. Nguyen, D. D. Sukachev, M. K. Bhaskar, B. Machielse, D. S. Levonian, E. N. Knall, P. Stroganov, R. Riedinger, H. Park, M. Lončar, and M. D. Lukin, Quantum network nodes based on diamond qubits with an efficient nanophotonic interface, *Phys. Rev. Lett.* **123**, 183602 (2019).
  - [37] P.-J. Stas, Y. Q. Huan, B. Machielse, E. N. Knall, A. Suleymanzade, B. Pingault, M. Sutula, S. W. Ding, C. M. Knaut, D. R. Assumpcao, Y.-C. Wei, M. K. Bhaskar, R. Riedinger, D. D. Sukachev, H. Park, M. Lončar, D. S. Levonian, and M. D. Lukin, Robust multi-qubit quantum network node with integrated error detection, *Science* **378**, 557 (2022).
  - [38] C. M. Knaut, A. Suleymanzade, Y. C. Wei, D. R. Assumpcao, P. J. Stas, Y. Q. Huan, B. Machielse, E. N. Knall, M. Sutula, G. Baranes, N. Sinclair, C. De-Eknamkul, D. S. Levonian, M. K. Bhaskar, H. Park, M. Lončar, and M. D. Lukin, Entanglement of nanophotonic quantum memory nodes in a telecom network, *Nature* **629**, 573 (2024).
  - [39] Y.-C. Wei, P.-J. Stas, A. Suleymanzade, G. Baranes, F. Machado, Y. Q. Huan, C. M. Knaut, S. W. Ding, M. Merz, E. N. Knall, U. Yazlar, M. Sirotin, I. W. Wang, B. Machielse, S. F. Yelin, J. Borregaard, H. Park, M. Lončar, and M. D. Lukin, Universal distributed blind quantum computing with solid-state qubits, *Science* **388**, 509 (2025).
  - [40] S. Schietinger, M. Barth, T. Aichele, and O. Benson, Plasmon-enhanced single photon emission from a nanoassembled metal-diamond hybrid structure at room temperature, *Nano Letters* **9**, 1694 (2009).
  - [41] Z. Wang, L. Balembois, M. Rančić, E. Billaud, M. Le Dantec, A. Ferrier, P. Goldner, S. Bertaina, T. Chanelière, D. Esteve, D. Vion, P. Bertet, and E. Flurin, Single-electron spin resonance detection by microwave photon counting, *Nature* **619**, 276 (2023).
  - [42] L.-M. Duan and H. J. Kimble, Scalable photonic quantum computation through cavity-assisted interactions, *Phys. Rev. Lett.* **92**, 127902 (2004).
  - [43] M. G. Raymer, C. Embleton, and J. H. Shapiro, The duan-kimble cavity-atom quantum memory loading scheme revisited, *Phys. Rev. Appl.* **22**, 044013 (2024).
  - [44] M. Pechal, L. Huthmacher, C. Eichler, S. Zeytinoglu, A. Abdumalikov, S. Berger, A. Wallraff, and S. Filipp, Microwave-Controlled Generation of Shaped Single Photons in Circuit Quantum Electrodynamics, *Physical Review X* **4**, 041010 (2014).
  - [45] C. Axline, L. Burkhardt, W. Pfaff, M. Zhang, K. Chou, P. Campagne-Ibarcq, P. Reinhold, L. Frunzio, S. M. Girvin, L. Jiang, M. H. Devoret, and R. J. Schoelkopf, On-demand quantum state transfer and entanglement between remote microwave cavity memories, *Nature Physics* **14**, 705 (2018).
  - [46] P. Campagne-Ibarcq, E. Zolys-Geller, A. Narla, S. Shankar, P. Reinhold, L. D. Burkhardt, C. J. Axline, W. Pfaff, L. Frunzio, R. J. Schoelkopf, and M. H. Devoret, Deterministic remote entanglement of superconducting circuits through microwave two-photon transitions, *Physical Review Letters* **120**, 200501 (2018).
  - [47] P. Kurpiers, P. Magnard, T. Walter, B. Royer, M. Pechal, J. Heinsoo, Y. Salathé, A. Akin, S. Storz, J.-C. Besse, S. Gasparinetti, A. Blais, and A. Wallraff, Deterministic Quantum State Transfer and Generation of Remote Entanglement using Microwave Photons, *Nature* **558**, 264 (2018).
  - [48] P. Kurpiers, M. Pechal, B. Royer, P. Magnard, T. Walter, J. Heinsoo, Y. Salathé, A. Akin, S. Storz, J.-C. Besse, S. Gasparinetti, A. Blais, and A. Wallraff, Quantum communication with time-bin encoded microwave photons, *Phys. Rev. Appl.* **12**, 044067 (2019).
  - [49] V. V. Dobrovitski, G. D. Fuchs, A. L. Falk, C. Santori, and D. D. Awschalom, Quantum Control over Single Spins in Diamond, *Annual Review of Condensed Matter Physics* **4**, 23 (2013), publisher: Annual Reviews.
  - [50] M. W. Doherty, N. B. Manson, P. Delaney, F. Jelezko, J. Wrachtrup, and L. C. L. Hollenberg, The nitrogen-vacancy colour centre in diamond, *Physics Reports* **528**, 1 (2013).
  - [51] M. Ruf, N. H. Wan, H. Choi, D. Englund, and R. Hanson, Quantum networks based on color centers in diamond, *Journal of Applied Physics* **130**, 070901 (2021).
  - [52] I. B. W. Harris, I. Christen, S. M. Patomäki, H. Raniwala, M. Sirotin, M. Colangelo, K. C. Chen, C. Errando-Herranz, D. J. Starling, R. Murphy, K. Shtyrkova, O. Medeiros, M. E. Trusheim, K. K. Berggren, P. B. Dixon, and D. Englund, High-fidelity control of a strongly coupled electro-nuclear spin-photon interface (2025), [arXiv:2505.09267 \[quant-ph\]](https://arxiv.org/abs/2505.09267).
  - [53] F. Böhm, N. Nikolay, S. Neinert, C. E. Nebel, and O. Benson, Ground-state microwave-stimulated raman transitions and adiabatic spin transfer in the  $^{15}\text{N}$  nitrogen vacancy center, *Phys. Rev. B* **104**, 035201 (2021).
  - [54] M. P. Bland, F. Bahrami, J. G. C. Martinez, P. H. Prestegard, B. M. Smitham, A. Joshi, E. Hedrick, A. Pakpour-Tabrizi, S. Kumar, A. Jindal, R. D. Chang, A. Yang, G. Cheng, N. Yao, R. J. Cava, N. P. de Leon, and A. A. Houck, 2d transmons with lifetimes and coherence times exceeding 1 millisecond (2025), [arXiv:2503.14798 \[quant-ph\]](https://arxiv.org/abs/2503.14798).
  - [55] L. Rondin, J.-P. Tetienne, T. Hingant, J.-F. Roch, P. Maletinsky, and V. Jacques, Magnetometry with

- nitrogen-vacancy defects in diamond, [Reports on Progress in Physics](#) **77**, 056503 (2014), publisher: IOP Publishing.
- [56] P. Haikka, Y. Kubo, A. Bienfait, P. Bertet, and K. Mølmer, Proposal for detecting a single electron spin in a microwave resonator, [Phys. Rev. A](#) **95**, 022306 (2017).
- [57] C. Eichler, A. J. Sigillito, S. A. Lyon, and J. R. Petta, Electron spin resonance at the level of  $10^4$  spins using low impedance superconducting resonators, [Phys. Rev. Lett.](#) **118**, 037701 (2017).
- [58] V. Ranjan, S. Probst, B. Albanese, T. Schenkel, D. Vion, D. Esteve, J. J. L. Morton, and P. Bertet, Electron spin resonance spectroscopy with femtoliter detection volume, [Applied Physics Letters](#) **116**, 184002 (2020).
- [59] X. Guo, N. Deegan, J. C. Karsch, Z. Li, T. Liu, R. Shreiner, A. Butcher, D. D. Awschalom, F. J. Heremans, and A. A. High, Tunable and transferable diamond membranes for integrated quantum technologies, [Nano Letters](#) **21**, 10392 (2021).
- [60] X. Guo, M. Xie, A. Addhya, A. Linder, U. Zvi, S. Wang, X. Yu, T. D. Deshmukh, Y. Liu, I. N. Hammock, Z. Li, C. T. DeVault, A. Butcher, A. P. Esser-Kahn, D. D. Awschalom, N. Deegan, P. C. Maurer, F. J. Heremans, and A. A. High, Direct-bonded diamond membranes for heterogeneous quantum and electronic technologies, [Nature Communications](#) **15**, 8788 (2024).
- [61] S. W. Ding, M. Haas, X. Guo, K. Kuruma, C. Jin, Z. Li, D. D. Awschalom, N. Deegan, F. J. Heremans, A. A. High, and M. Loncar, High-q cavity interface for color centers in thin film diamond, [Nature Communications](#) **15**, 6358 (2024).
- [62] J. I.-J. Wang, M. A. Yamoah, Q. Li, A. H. Karamlou, T. Dinh, B. Kannan, J. Braumüller, D. Kim, A. J. Melville, S. E. Muschinske, B. M. Niedzielski, K. Serniak, Y. Sung, R. Winik, J. L. Yoder, M. E. Schwartz, K. Watanabe, T. Taniguchi, T. P. Orlando, S. Gustavsson, P. Jarillo-Herrero, and W. D. Oliver, Hexagonal boron nitride as a low-loss dielectric for superconducting quantum circuits and qubits, [Nature Materials](#) **21**, 398 (2022).
- [63] J. Verjauw, A. Potočník, M. Mongillo, R. Acharya, F. Mohiyaddin, G. Simion, A. Pacco, T. Ivanov, D. Wan, A. Vanleenhove, L. Souriau, J. Jussot, A. Thiam, J. Swerts, X. Piao, S. Couet, M. Heyns, B. Govoreanu, and I. Radu, Investigation of microwave loss induced by oxide regrowth in high-q niobium resonators, [Phys. Rev. Appl.](#) **16**, 014018 (2021).
- [64] R. N. Simons, Conductor-backed coplanar waveguide, in [Coplanar Waveguide Circuits, Components, and Systems](#) (John Wiley & Sons, Ltd, 2001) Chap. 3, pp. 87–111.
- [65] J. N. Sahalos and G. A. Kyriacou, [Tunable Materials with Applications in Antennas and Microwaves](#) (Springer Cham, 2019).
- [66] A. J. Annunziata, D. F. Santavicca, L. Frunzio, G. Cate-lani, M. J. Rooks, A. Frydman, and D. E. Prober, Tunable superconducting nanoinductors, [Nanotechnology](#) **21**, 445202 (2010).
- [67] C. R. H. McRae, H. Wang, J. Gao, M. R. Vissers, T. Brecht, A. Dunsworth, D. P. Pappas, and J. Mutus, Materials loss measurements using superconducting microwave resonators, [Review of Scientific Instruments](#) **91**, 091101 (2020).
- [68] D. Kowsari, K. Zheng, J. T. Monroe, N. J. Thobaben, X. Du, P. M. Harrington, E. A. Henriksen, D. S. Wisbey, and K. W. Murch, Fabrication and surface treatment of electron-beam evaporated niobium for low-loss coplanar waveguide resonators, [Applied Physics Letters](#) **119**, 132601 (2021).
- [69] B. N. R. Lap, A. Khudchenko, R. Hesper, K. I. Rudakov, P. Dmitriev, F. Khan, V. P. Koshelets, and A. M. Baryshev, Characterization of superconducting nbtin films using a dispersive fourier transform spectrometer, [Applied Physics Letters](#) **119**, 152601 (2021).
- [70] B. Yurke and J. S. Denker, Quantum network theory, [Phys. Rev. A](#) **29**, 1419 (1984).
- [71] D. M. Pozar, [Microwave engineering](#), 4th ed. (Wiley, 2012).
- [72] A. Reiserer and G. Rempe, Cavity-based quantum networks with single atoms and optical photons, [Rev. Mod. Phys.](#) **87**, 1379 (2015).
- [73] A. Reiserer and G. Rempe, Cavity-based quantum networks with single atoms and optical photons, [Rev. Mod. Phys.](#) **87**, 1379 (2015).
- [74] B. C. Rose, D. Huang, Z.-H. Zhang, P. Stevenson, A. M. Tyryshkin, S. Sangtawesin, S. Srinivasan, L. Loudin, M. L. Markham, A. M. Edmonds, D. J. Twitchen, S. A. Lyon, and N. P. de Leon, Observation of an environmentally insensitive solid-state spin defect in diamond, [Science](#) **361**, 60 (2018).
- [75] Z.-H. Zhang, P. Stevenson, G. m. H. Thiering, B. C. Rose, D. Huang, A. M. Edmonds, M. L. Markham, S. A. Lyon, A. Gali, and N. P. de Leon, Optically detected magnetic resonance in neutral silicon vacancy centers in diamond via bound exciton states, [Phys. Rev. Lett.](#) **125**, 237402 (2020).
- [76] M. K. Bhaskar, [Diamond nanophotonic quantum networks](#), Ph.D. thesis, Harvard University (2021).
- [77] A. Alkauskas, B. B. Buckley, D. D. Awschalom, and C. G. Van de Walle, First-principles theory of the luminescence lineshape for the triplet transition in diamond nv centres, [New Journal of Physics](#) **16**, 073026 (2014).
- [78] A. Faraon, P. E. Barclay, C. Santori, K.-M. C. Fu, and R. G. Beausoleil, Resonant enhancement of the zero-phonon emission from a colour centre in a diamond cavity, [Nature Photonics](#) **5**, 301 (2011).



A	Methods	9
1	Microwave Resonator Modeling	9
2	Analysis on zero-point current fluctuations and Finite-Element Simulation	9
3	Microwave Circuit Parameter Analysis	11
4	Microwave Resonator–Spin Coupling Rate	12
5	Metal-Induced Optical Loss Simulation	12
B	Figures of Merit at Different Spin Locations	13
C	Spin-Photon Entanglement Schemes	13
1	Amplitude-Based Scheme	15
2	Phase-Shift Scheme	15
D	Entanglement Fidelity of Microwave Retrieval	17
E	Scheme Compatible Color Centers	18
1	Perturbation Calculation of the Magnetic Dipole Moment of $^{117}\text{SnV}^-$	18
2	Optical Cooperativity Estimation for $\text{NV}^-$	19
F	Intrinsic Heralding Rate Estimation	20

## Appendix A: Methods

### 1. Microwave Resonator Modeling

We analyze our microwave resonator using a finite-element simulator, Sonnet v19.52 (Sonnet Software Inc.). For implementation, we considered a three-layer structure enclosed in a perfect conductor box. The bottom layer is a sapphire wafer with a thickness of 200  $\mu\text{m}$ . On top of it, a superconducting LC circuit along with a coplanar waveguide is patterned. This layer is set as a 100 nm thick diamond. We used a conductor-backed coplanar waveguide structure to achieve  $Z_0 = 50 \Omega$  [64, 65]. To realize the diamond-sandwiched parallel-plate capacitor structure, a superconducting metal layer covering the LC circuit area is drawn at the bottom of the third layer, which is air with a thickness of 10 mm.

In designing the microwave resonator, it is essential to account for the kinetic inductance arising from the inertia of Cooper pairs in the superconducting film [56, 66]. In recent implementations of superconducting circuits, a 200 nm-thick niobium film remains an excellent choice for achieving high internal quality factors [67, 68]. Within BCS theory, the sheet kinetic inductance is given by [66]

$$L_{K,\square} = \frac{R_{\square}\hbar}{\pi\Delta} \coth\left(\frac{\Delta}{2k_B T}\right), \quad (\text{A1})$$

where  $R_{\square}$  is the normal-state sheet resistance,  $\Delta$  is the superconducting energy gap, and  $k_B$  is the Boltzmann constant. For 200 nm-thick niobium film,  $R_{\square} = 0.49 \Omega$  [68] and  $\Delta = 1.4 \text{ meV}$  [69] yield  $L_{K,\square} = 0.073 \text{ pH/sq}$ .

### 2. Analysis on zero-point current fluctuations and Finite-Element Simulation

In this section, we describe our method to extract the zero-point current fluctuations directly from finite-element simulation results without relying on explicit mapping to a lumped-element circuit. The conventional approach for obtaining  $\delta I$  is to infer the characteristic impedance  $Z$  by fitting the simulated response to an equivalent lumped-element model. This is typically done by varying the participation of an inductive element or by comparing current ratios to deduce an equivalent lumped-element impedance  $Z$  [57]. The problem is that microwave circuits do not operate in a strong lumped-element limit where components can be accurately approximated as ideal inductors or capacitors. For example, commonly used interdigitated capacitors introduce substantial stray inductance due to their extended finger geometry, altering the total circuit inductance and thereby leading to inaccurate estimates of the current fluctuations at the spin location. To avoid such issues, we introduce a method that computes the zero-point current fluctuations directly from the simulated current response and scattering parameters, eliminating the need for any lumped-element model extraction.

Let us denote the current at port 1 as  $I_{\text{in}}$  and at the inductive wire as  $I_L$  (Fig. 3(a)). From the Wiener–Khinchin theorem,

$$\delta I^2 = \langle I_L^2(0) \rangle = \int_{-\infty}^{\infty} |I_L(\omega)|^2 \frac{d\omega}{2\pi} \quad (\text{A2})$$

$$= 2 \int_{-\infty}^{\infty} |\chi_{II}(\omega)|^2 S_{++}(\omega) \frac{d\omega}{2\pi}, \quad (\text{A3})$$

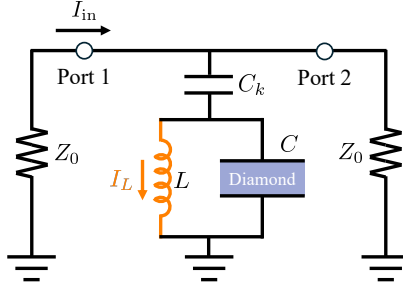


FIG. 4. Effective circuit diagram of the resonator coupled to a coplanar waveguide (CPW) transmission line. The circuit is conceptually equivalent to the model in Ref. [57].

where

$$S_{++}(\omega) = \frac{\hbar\omega}{2Z_0} \quad (\text{A4})$$

is the power spectral density of the incoming current fluctuations in port 1 [70]. The factor of two in Eq. A3 accounts for the zero-point fluctuations entering from port 2, which by symmetry are equal to those generated by those at port 1.

In the high quality factor limit,  $\chi_{II}(\omega)$  is sharply peaked at the resonance frequency, enabling the frequency dependence of  $S_{++}(\omega)$  to be neglected. Eq. A3 can then be approximated as

$$\delta I^2 = \frac{\hbar\omega_R}{2Z_0} \int_{-\infty}^{\infty} 2 |\chi_{II}(\omega)|^2 \frac{d\omega}{2\pi}. \quad (\text{A5})$$

To apply this analysis to the Sonnet simulation results, it is required to extract  $I^+$  from  $I_{\text{in}}$ . The total current at port 1 is  $I_{\text{in}} = I^+ - I^-$ , where  $I^-$  is the reflected current which can be obtained from the scattering matrix as  $I^- = S_{11}I^+$  [71]. Therefore,

$$I_{\text{in}} = (1 - S_{11})I^+. \quad (\text{A6})$$

Expressing the  $\chi_{II}$  in terms of  $I_{\text{in}}$ , we obtain

$$\chi_{II} = \frac{I_L}{I_{\text{in}}} (1 - S_{11}). \quad (\text{A7})$$

Substituting Eq. (A7) into Eq. (A5) yields

$$\delta I^2 = \frac{\hbar\omega_R}{2Z_0} \int_{-\infty}^{\infty} 2 \left| \frac{I_L(\omega)}{I_{\text{in}}(\omega)} \right|^2 |1 - S_{11}|^2 \frac{d\omega}{2\pi}. \quad (\text{A8})$$

This equation is useful because it gives the zero-point current fluctuations directly from simulation results.

As a check, we show that this expression leads to  $\delta I = \omega_R \sqrt{\frac{\hbar}{2Z}}$  for an LC circuit with characteristic impedance  $Z$ . Fig. 4 shows the effective circuit of the resonator coupled to the CPW, which is conceptually equivalent to the model in Ref. [57]. Defining the impedance seen from port 1 as  $Z_R$ , we obtain

$$\frac{1}{Z_R} = \frac{1}{Z_0} + \frac{1}{Z_k}, \quad (\text{A9})$$

where

$$Z_k = \frac{1}{i\omega C_k} + \frac{i\omega L}{1 - \omega^2 LC}.$$

The reflection coefficient is  $S_{11}$  [71],

$$S_{11} = \frac{Z_R - Z_0}{Z_R + Z_0} \rightarrow 1 - S_{11} = \frac{2Z_0}{Z_R + Z_0}. \quad (\text{A10})$$

The fraction of the input current  $I_{\text{in}}$  that flows into the inductive wire ( $I_L$ ) is determined by the impedance relation, given by

$$\frac{I_L}{I_{\text{in}}} = \frac{Z_0}{Z_0 + Z_k} \frac{1}{1 - \omega^2 LC}. \quad (\text{A11})$$

We now introduce the dimensionless variables

$$Z' = \frac{Z_k}{Z_0}, \quad \omega' = \frac{\omega}{\omega_R}, \quad C' = \omega_R Z_0 C_k, \quad L' = \frac{\omega_R L}{Z_0},$$

which yield

$$\begin{aligned} Z' &= \frac{1}{i\omega' C'} + \frac{i\omega' L'}{1 - \omega'^2}, \\ 1 - S_{11} &= 1 + \frac{1}{2Z' + 1}, \\ \frac{I_L}{I_{\text{in}}} &= \frac{1}{1 + Z'} \frac{1}{1 - \omega'^2}. \end{aligned}$$

Thus, the current-current susceptibility becomes

$$\chi_{II}(\omega') = \frac{2\omega' C'}{2i - \omega' C' - 2i\omega'^2(1 + L' C') + \omega'^3 C'}.$$

Expanding  $1/\chi_{II}$  for  $\omega'$  about the point  $1/\sqrt{1 + L' C'}$  gives

$$\frac{1}{\chi_{II}} = \frac{L' C'}{2 + 2L' C'} + \left( \frac{2i}{C'} + 2iL' - \frac{1}{\sqrt{1 + L' C'}} \right) \left( \omega' - \frac{1}{\sqrt{1 + L' C'}} \right) + 0 \cdot \left( \omega' - \frac{1}{\sqrt{1 + L' C'}} \right)^2 + \dots$$

In the limit  $C' \rightarrow 0$ ,

$$\chi_{II}(\omega') \approx \frac{\frac{C'}{2 + 2L' C'}}{\frac{L' C'^2}{(2 + 2L' C')^2} + i \left( \omega' - \frac{1}{\sqrt{L' C'}} \right)} \approx \frac{2}{L' C'} \frac{\frac{L' C'^2}{4}}{\frac{L' C'^2}{4} + i \left( \omega' - \frac{1}{\sqrt{L' C'}} \right)},$$

where the last part is a Lorentzian form. The integral of the  $|\chi_{II}(\omega')|^2$  is then,

$$\int_{-\infty}^{\infty} |\chi_{II}(\omega')|^2 \frac{d\omega'}{2\pi} \approx \frac{1}{2L'} \rightarrow \omega_R \frac{Z_0}{2\omega_R L} = \frac{Z_0}{Z} \frac{\omega_R}{2},$$

where the final step restores the original frequency and inductance units. Therefore,

$$\delta I^2 = \frac{\hbar \omega_R}{Z_0} \cdot \frac{Z_0}{Z} \frac{\omega_R}{2} = \omega_R^2 \frac{\hbar}{2Z}, \quad (\text{A12})$$

which gives the zero-point current fluctuations of the resonator:

$$\delta I = \omega_R \sqrt{\frac{\hbar}{2Z}}. \quad (\text{A13})$$

### 3. Microwave Circuit Parameter Analysis

From the simulation data, we obtain  $\omega_R$  and  $\delta I$ , which are all expressed in terms of circuit inductance  $L$  and capacitance  $C$ . Therefore, it is possible to extract circuit parameters from the simulation data,

$$C = \frac{1}{\omega_R Z} = \frac{2\delta I^2}{\hbar \omega_R^3}, \quad (\text{A14})$$

$$L = \frac{Z}{\omega_R} = \frac{\hbar \omega_R}{2\delta I^2}. \quad (\text{A15})$$

$L$ (pH)	$C$ (pF)	$C_{\text{cal}}$ (pF)
7.03	1.16	1.27
6.69	5.03	5.10
6.70	11.49	11.47
6.75	20.55	20.40

TABLE II. Simulated circuit parameters ( $L$  and  $C$ ) and calculated capacitance  $C_{\text{cal}}$  for a microwave resonator with a fixed inductive wire ( $2\ \mu\text{m} \times 0.1\ \mu\text{m}$ ) and varying capacitor area.

For the test circuit with two capacitor pads (1 mm by 2 mm) on level 1 connected by an inductive wire of length 250  $\mu\text{m}$  and 5  $\mu\text{m}$  wide with level 3 metal covering the wire region as well,  $C = 503\ \text{pF}$  and  $L = 15.48\ \text{pH}$ , which matches very well with the capacitance of the parallel-plate capacitor with dielectric constant  $\epsilon_r = 5.76$ , which is expected to be 510 pF. The inductance of a wire covered by a superconducting pad can be simulated in Sonnet by setting two ports on each side of inductive wire and applying basic inductance measurement model. This simulation predicts inductance of 13.2 pH, matches well with the  $L$  obtained. Changing the inductive wire geometry to 50  $\mu\text{m}$  long and 5  $\mu\text{m}$  wide, this LC circuit gives  $C = 504\ \text{pF}$  and  $L = 4.92\ \text{pH}$ , where the wire inductance is expected to be 2.64 pH. These results show that our analysis matched with the expected results and the circuit inductance is dominated by the wire inductance.

Next, we examine whether the stray inductance scales with the capacitor size. Using a fixed inductive wire geometry (length 2  $\mu\text{m}$ , width 0.1  $\mu\text{m}$ ), Table II summarizes the simulated circuit parameters for increasing capacitor area. Here,  $L$  and  $C$  are obtained from Sonnet simulations, while  $C_{\text{cal}}$  is the capacitance estimated from the ideal parallel-plate capacitor expression. The results show that the inductance  $L$  remains nearly constant even as the capacitance increases, demonstrating that the stray inductance does not scale with the capacitor size. This confirms that the dominant contribution to the total inductance originates from the inductive wire rather than the capacitor geometry.

#### 4. Microwave Resonator–Spin Coupling Rate

The microwave coupling rate is given by [56]

$$g_m = -\gamma_e \delta \mathbf{B} \cdot \langle 0|\mathbf{S}|1\rangle, \quad (\text{A16})$$

where  $\gamma_e/2\pi = 28\ \text{GHz/T}$  is the electron gyromagnetic ratio,  $\delta \mathbf{B}$  denotes the zero-point magnetic field fluctuations, and  $\langle 0|\mathbf{S}|1\rangle$  is the spin transition matrix element. The field  $\delta \mathbf{B}$  is evaluated using the Biot–Savart law with the zero-point current fluctuations  $\delta I$ . The magnetic dipole moment  $\gamma_e \langle 0|\mathbf{S}|1\rangle$  depends on the specific spin system, as summarized in Table V.

#### 5. Metal-Induced Optical Loss Simulation

Our optical cavity design is based on the high quality factor photonic crystal (PhC) cavity demonstrated in Ref. [61], where the PhC cavity is suspended in air to maximize vertical optical confinement and minimize substrate losses. In contrast, our device employs a substrate-supported geometry optimized for integration with the superconducting microwave circuit, as shown in Fig. 3. Specifically, the multilayer stack consists of a 200  $\mu\text{m}$  thick sapphire substrate, a 200 nm thick niobium film, and a diamond membrane structured such that the niobium region retains 100 nm of diamond while the optical cavity region preserves 300 nm. A second 200 nm thick niobium layer is subsequently deposited atop the 100 nm diamond region. The overall PhC slab geometry is 300 nm thick and 200 nm wide.

To accommodate this geometry, we optimized the photonic crystal parameters for  $\text{SnV}^-$  to  $a = 0.1925\ \mu\text{m}$ ,  $r = 48\ \text{nm}$ , and a minimum taper size of  $a \times 0.8845$  in the cavity region, using quadratic tapering over six periods [61]. The resulting cavity supports a TM-like mode, in contrast to the TE-like mode in Ref. [61], thus minimizing evanescent field overlap with the nearby metal layer. Finite-difference time-domain simulations were performed using Tidy3D to evaluate the optical properties. Metal-induced losses were included by modeling the superconducting region as gold. When the cavity edge was positioned 500 nm from the metal edge, the simulated quality factor was  $Q = 1.86 \times 10^4$ , which corresponds to the intrinsic decay rate  $\kappa_{o,i}/2\pi = 25.8\ \text{GHz}$ . For other cavity–metal separations  $d$  (in nm), the corresponding values of  $\kappa_{o,i}$  (in GHz) are  $(d, \kappa_{o,i}/2\pi) = (200, 36.5)$ ,  $(150, 77.7)$ , and  $(100, 230)$ .

To evaluate the cooperativity of our optical cavity, we require three quantities: the cavity coupling rate  $g_o$ , the



Color Center	Location	$C$	$g_m/2\pi$ (kHz)	Heralding Probability	Fidelity
$^{117}\text{SnV}^-$	A	157	0.630	17.1%	0.929
	B	112	0.767	19.8%	
	C	43.1	0.904	21.8%	
$\text{NV}^-$	A	18.0	3.18	39.6%	0.900
	B	12.8	3.78	39.6%	
	C	4.94	4.35	32.7%	
$\text{SiV}^0$	A	845	2.10	37.7%	0.949
	B	601	2.55	40.9%	
	C	232	3.01	43.0%	

TABLE III. Heraldng probability for spins with different optical cooperativity  $C$  and microwave coupling rate  $g_m$ . The detection time is fixed at 107  $\mu\text{s}$ , which yields a fidelity of 0.9 for the  $\text{NV}^-$  center. The transmon lifetime is taken to be  $T_{1,t} = 1$  ms [54].

cavity decay rate  $\kappa_o$ , and the emitter decay rate  $\gamma_o$ . The cavity coupling rate is given by [72]

$$g_o(\vec{r}) = \frac{\mu E}{\hbar} = \sqrt{\frac{\mu^2 \omega_o}{2\epsilon_0 \hbar V}} u(\vec{r}),$$

where

$$u(\vec{r}) = \sqrt{\frac{\epsilon(\vec{r}) |E(\vec{r})|^2}{\max[\epsilon(\vec{r}) |E(\vec{r})|^2]}},$$

$$V = \int u(\vec{r})^2 d^3r.$$

Here,  $\mu$  is the electric dipole moment,  $\omega_o$  is the optical cavity frequency,  $\epsilon_0$  is the vacuum permittivity,  $\epsilon(\vec{r})$  is cavity permittivity distribution, and  $E(\vec{r})$  is the cavity electric-field profile. From the optical cavity simulations, we obtain  $\epsilon(\vec{r})$ ,  $E(\vec{r})$ , and the cavity loss rate  $\kappa_o$ . We considered critical coupling, taking  $\kappa_o = \kappa_{o,i} + \kappa_{o,e} \approx 2\kappa_{o,i}$ , where  $\kappa_{o,e}$  is the extrinsic decay rate. The spin-dependent quantities are the dipole moment  $\mu$  and the optical decay rate  $\gamma_o$ , given by

$$\mu = \sqrt{\frac{3\pi\epsilon_0 \hbar c^3}{n\omega^3 \tau_{\text{rad}}}},$$

$$\gamma_o = \frac{1}{\tau_{\text{rad}} * \xi},$$

where  $c$  is the speed of light,  $n$  is the refractive index (for diamond,  $n = 2.4$ ),  $\omega$  is the zero phonon line (ZPL) transition frequency,  $\tau_{\text{rad}}$  is the radiative lifetime, and  $\xi$  is the Debye-Waller factor. The definition of  $\gamma_o$  is discussed in Sec. E 2. The parameters used in our calculation are listed in Table V. The resulting optical cooperativity  $C = g_o^2/\kappa_o\gamma_o$  is plotted in Fig. 3 of the main text and in Fig. 5 of the Supplementary Information.

## Appendix B: Figures of Merit at Different Spin Locations

As the optical cavity approaches the microwave resonator, metal-induced losses increase, leading to a rapid degradation of the optical cooperativity. In contrast, the microwave coupling rate  $g_m$  decreases as the spin is positioned farther from the resonator. Therefore, optimizing both the cavity placement and the spin location is crucial for achieving optimal device performance for pump-free quantum transduction. Fig. 5 presents the calculated heralding efficiency and fidelity for various spin positions (marked as stars) within the optical cavity. Results are shown for three different kinds of color centers. Table III lists the heralding efficiency values for selected spin positions in Fig. 5, where the detection time is fixed to 107  $\mu\text{s}$  which is the time for the NV center to stay in 90% fidelity.

## Appendix C: Spin-Photon Entanglement Schemes

The spin-photon entanglement is created by spin-dependent optical reflection. In the setting of cavity quantum electrodynamics (cavity QED), an atom couples to a cavity mode through the Jaynes-Cummings Hamiltonian. Using

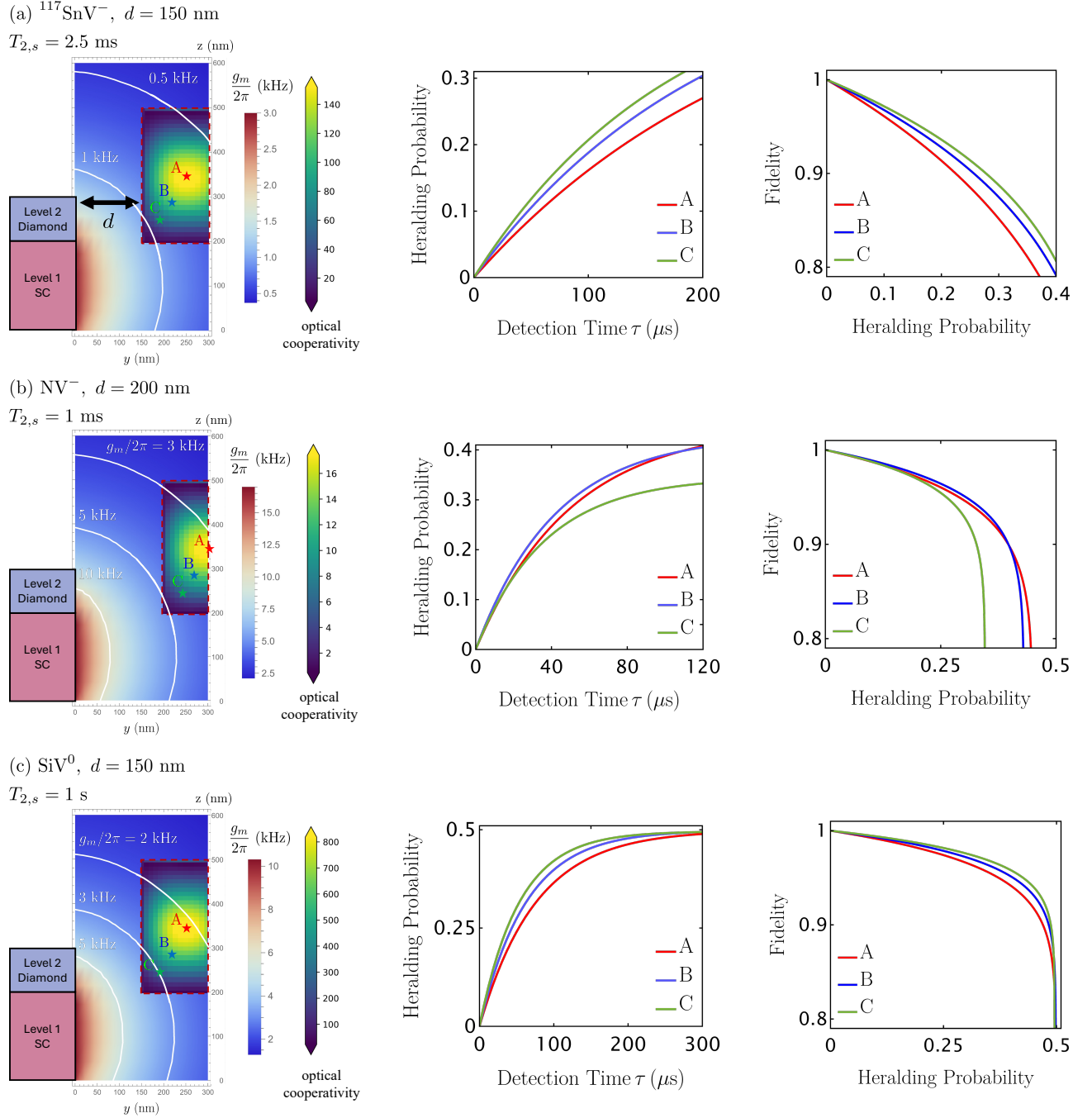


FIG. 5. Figures of merit for selected spin positions (indicated by stars) in the optical cavity, evaluated for different color centers.

the input-output relation, a photon impinging on the cavity gets reflected depending on its carrier frequency  $\omega$  by [73]

$$\mathcal{R}(\omega) = |r(\omega)|^2 = \left| 1 - \frac{2\kappa_c}{i(\omega - \omega_c) + \kappa + g^2/(i(\omega - \omega_a) + \gamma)} \right|^2, \quad (\text{C1})$$

where  $\omega_c$  and  $\omega_a$  are the resonance frequencies of the cavity and the two-level atom, respectively. The  $g$  describes the atom-cavity coupling strength;  $\gamma$  is the atom's spontaneous decay rate in free space. The cavity couples to the environment with a rate  $\kappa_c$  and has an internal loss rate of  $\kappa_i$ . The total loss rate is  $\kappa = \kappa_i + \kappa_c$ .

There are two different reflection schemes: amplitude-based [35] and phase-shift-based [42, 43]. Both schemes require strong spin-photon interaction with high cooperativity  $C = \frac{g^2}{\kappa\gamma} \gg 1$ . In the amplitude-based protocol, one spin

TABLE IV. Comparison between three different spin-photon entanglement schemes. In the phase-shift schemes, the performance metrics are expanded around small intrinsic loss rate  $\kappa_i/\kappa_c$ . Following the convention in [43], the cooperativity  $\mathcal{C} = g^2/\kappa_c\gamma$  is used in the context of phase-shift scheme.  $G(t)$  is given by the input pulse shape.

	Amplitude-based	Phase-shift (on-off)	Phase-shift (push-pull)
Success Probability	$0.5 \frac{C^2}{(C+1)^2} - O(\frac{\Delta^2}{\kappa^2})$	$\frac{3}{4} + \frac{(C-1)^2}{4(C+1)^2} - O(\frac{\kappa_i}{\kappa_c})$	$\frac{\mathcal{C}}{1+\mathcal{C}} - O(\frac{\kappa_i}{\kappa_c})$
State Fidelity	$1 - O(\frac{\gamma}{\kappa})$	$\frac{(1+2C)^2}{4(1+C+C^2)} - O(\frac{\kappa_i}{\kappa_c})$	$\frac{\mathcal{C}+\sqrt{-1+C^2}}{2C} - O(\frac{\kappa_i}{\kappa_c})$
Waveform Distortion	Irrelevant	$ G_0 r_{\text{ON/OFF}}(0) - \pi \ddot{G}(0) r''_{\text{ON/OFF}}(0) ^2$	$ G_0 r_{\pm}(0) - \pi \ddot{G}(0) r''_{\pm}(0) ^2$

state results in high reflectivity  $\mathcal{R}_{\text{max}} = 1$ , and the other spin state results in a non-reflective  $\mathcal{R}_{\text{min}} = 0$ , which basically carves out a Bell state from the initial spin-photon state. More specifically, the protocol starts with a spin-photon initial state of  $1/2(|E\rangle + |L\rangle)(|0\rangle + |1\rangle)$ , where  $E$  and  $L$  denote the early and late time bins of the photon state. 0 and 1 denote the spin qubit states. Suppose the  $|0\rangle$  state is highly reflective, and  $|1\rangle$  is non-reflective. The state after the reflection of the first time-bin is  $1/\sqrt{3}(|E\rangle|0\rangle + |L\rangle(|0\rangle + |1\rangle))$ . Inserting a  $\pi$ -pulse on the spin states between the two time bins, the state after the reflection of the late time bin is  $1/\sqrt{2}(|E\rangle|1\rangle + |L\rangle|0\rangle)$ . The fidelity of the final Bell state depends critically on the non-reflective state  $\mathcal{R}_{\text{min}} = 0$ . The success probability of scheme depends on  $\mathcal{R}_{\text{max}}$ .

In the phase-shift-based scheme, the two spin states reflect with a phase difference of  $\pi$ . In the original protocol [42], the initial state is prepared in  $1/2(|H\rangle + |V\rangle)(|0\rangle + |1\rangle)$ , where the  $H$  and  $V$  denote horizontally polarized and vertically polarized states of a photon. Here, 0 and 1 denote the spin qubit states. The vertically polarized photon does not enter the cavity, so the cavity only modifies the reflection of the horizontally polarized photon. The  $|0\rangle$  state creates a  $\pi$  phase shift on the reflected state, whereas the  $|1\rangle$  state does not. So the final state after reflection is  $1/2(-|H\rangle|0\rangle + |H\rangle|1\rangle + |V\rangle|0\rangle + |V\rangle|1\rangle)$ . In the more recent paper [43], the authors refer to the original scheme as the “on-off” scheme and propose a more symmetric phase-shift scheme: the “push-pull” scheme. The proposed scheme starts with the same initial state. The  $|0\rangle$  and  $|1\rangle$  spin states imprint  $\pm\pi/2$  phase-shift on the reflected state, resulting in the final entangled state  $1/2(-i|H\rangle|0\rangle + i|H\rangle|1\rangle + |V\rangle|0\rangle + |V\rangle|1\rangle)$ . The successful creation of phase contrast relies on a high-Q cavity and the designed detuning between the two spin states and the cavity.

In the main text, we focus on the amplitude-based scheme, but we can also apply the phase-shift based scheme for a higher overall entangling rate. The performance of the schemes depends on the cooperativity of the system. We summarize and compare the schemes in Table IV. In short, the phase-shift scheme, compared with the amplitude-based scheme, creates Bell pairs with a higher success probability and lower fidelity. In addition, the phase-shift scheme receives infidelity contribution from the photon wavepacket distortion, which affects the photon interference.

### 1. Amplitude-Based Scheme

The scheme works in the nearly critically coupled ( $\kappa_c \sim \kappa_i$ ), nearly resonant regime. Denoting the atom-cavity detuning to be  $\Delta_a = \omega_a - \omega_c$ , the hierarchy of parameters follows  $\gamma < g < \Delta_a < \kappa \ll \omega_c$ , where the atom locally modifies the cavity reflection spectrum [35].

In our protocol, we ensure that  $\mathcal{R}_{\text{min}} = 0$  to guarantee the generation of unit-fidelity spin-photon Bell state. The deviation from this condition, is roughly captured by imbalance between the loss rate as  $\mathcal{R}_{\text{min}} = (\kappa_c - \kappa_i)^2/\kappa^2 + O(\gamma/\kappa)$ . Satisfying the non-reflective condition on the zero-th order (which means critically coupled  $\kappa_c = \kappa_i$ ), the maximal reflection point can be shown to be  $\mathcal{R}_{\text{max}} = C^2/(C+1)^2 + O(\Delta_a^2/\kappa^2)$ , where the cooperativity has the convention  $C = g^2/\kappa\gamma$ . In the usual emitter-cavity system, where the atom decays through the cavity creating a single photon, the efficiency is given by  $C/(C+1)$  [73]. Here, the square in the high-reflection formula comes from the fact that atom has to absorb the photon and then re-emit.

The amplitude-based scheme has the advantage that it can guarantee unit Bell fidelity, however, due to the non-reflective state, the probability of successfully creating a spin-photon Bell state is bounded by 0.5, resulting in the final success probability to be  $P = 0.5 \cdot C^2/(C+1)^2$ . To get rid of the inefficiency, we may consider the phase-shift protocol.

### 2. Phase-Shift Scheme

Since the phase-shift scheme creates entanglement by phase difference, instead of erasing part of the state, the scheme achieves unit success probability in the high cooperativity ( $C \gg 1$ ), over-coupled ( $\kappa_c \gg \kappa_i$ ) regime [42, 43].

In the original spin-photon entanglement protocol, one requires two different spin transitions. One transition is on resonance with the cavity frequency, creating atom-cavity dressed state; the other transition is far off-resonant, effectively creating an “empty cavity”. The incoming photon at the cavity frequency will enter the “empty cavity” and bounce off the dressed state, creating an effective  $\pi$ -phase difference between these two cases. If we denote the reflection coefficient of the on-resonance condition to be  $r_{\text{ON}}(\omega)$  and the off-resonance condition to be  $r_{\text{OFF}}(\omega)$ , the “on-off” scheme ideally realizes  $|\arg(r_{\text{ON}}(\omega)) - \arg(r_{\text{OFF}}(\omega))| = \pi$ . In real experiments, the reflection is constrained by the cavity cooperativity and intrinsic loss. Following the convention in [43],

$$r_{\text{ON}} = \frac{(1 - \kappa_i/\kappa_c) - \mathcal{C}}{(1 + \kappa_i/\kappa_c) + \mathcal{C}}, \quad r_{\text{OFF}} = \frac{1 - \kappa_i/\kappa_c}{1 + \kappa_i/\kappa_c},$$

where  $\mathcal{C} = g^2/\kappa_c\gamma$  is the cooperativity defined only using the coupling loss. The probability of generating a Bell pair using this scheme is estimated to be  $P = 1/4((r_{\text{ON}})^2 + (r_{\text{OFF}})^2 + 2)$ . The fidelity is given by  $F = (-r_{\text{ON}} + r_{\text{OFF}} + 2)^2/16P$ . We can expand the expression for the probability and fidelity in the small intrinsic loss regime, and the result is summarized in Table IV. In the lossless limit, the success probability is shown to be greater than 3/4, exceeding the highest achievable probability of 1/2 of the amplitude-based scheme.

Despite a higher probability of success, one drawback of the scheme is that  $|r_{\text{ON}}(\omega)| = |r_{\text{OFF}}(\omega)|$  is usually not guaranteed, thus contributing to infidelity in the final Bell state. To overcome this issue, a more symmetric scheme uses two transitions  $\pm\Delta$  detuned from the cavity resonance. This design contributes to equal and opposite phase shifts of  $\pm\pi/2$  on the incoming photon at zero detuning  $\omega = \omega_c$  as long as the detuning satisfies  $\Delta^2/\gamma^2 = ((\mathcal{C} + \kappa_i^2/\kappa_c^2) - 1)/(1 - \kappa_i^2/\kappa_c^2)$  [43]. The  $\pm\Delta$  detuned states result in reflection coefficients  $r_-(\omega)$  and  $r_+(\omega)$  respectively, and it is guaranteed that  $|r_-(\omega_c)| = |r_+(\omega_c)|$ , as shown in [43]:

$$r_{\pm} = \pm i\Delta \frac{\sqrt{\gamma^2\kappa_c^2 + \Delta^2(\kappa_c^2 - \kappa_i^2)} - \gamma\kappa_c}{\Delta^2(\kappa_c + \kappa_i)}. \quad (\text{C2})$$

The probability and fidelity are similarly given by  $P = 1/4(|r_+|^2 + |r_-|^2 + 2)$  and  $F = (-ir_+ + ir_- + 2)^2/16P$ . We can again expand to see the leading order behavior of the scheme in Table IV. The comparison shows that in the  $\mathcal{C} \gg 1$  regime, the fidelity of the push-pull scheme upper bounds that of the on-off scheme.

Compared with the amplitude-based scheme, one additional concern for the phase-shift scheme is waveform distortion. The phase-shift scheme interferes a photon reflected from the cavity and a photon reflected from the mirror. It is important for photons to be indistinguishable. This is not a problem for the amplitude-based scheme, since all the outgoing photons are reflected in the same way by the cavity-atom system. Such waveform distortion can also be factored into the decrease in Bell state fidelity. In the above fidelity estimation, this distortion contribution is neglected because we fix the incoming photon frequency. To see the waveform distortion, we need the response of the atom-cavity system to a photon wave-packet. Suppose the incoming photon pulse has a smooth temporal shape given by  $f(t)$  (e.g. a Gaussian pulse). Its spectrum is given by the Fourier transform  $\mathcal{F}[f(t)] = f(\omega)$ . After the reflection, the pulse’s waveform in frequency domain is altered by  $r(\omega)f(\omega)$ . To quantify the amount of distortion, we calculate the overlap between the reflected signal waveform and the original waveform:

$$F_{\text{signal}} = \left| \int_{-\infty}^{\infty} r(\omega) |f(\omega)|^2 d\omega \right|^2, \quad (\text{C3})$$

where we assume  $f(\omega)$  is square-normalized. Given  $r(\omega)$  of the system, the distortion is minimized when the input signal is mono-frequency (i.e. a Dirac delta function in the frequency domain). For an arbitrary input signal  $f(t)$ , we can estimate  $F_{\text{signal}}$  in the following way. Find the function  $G(t)$  such that  $\mathcal{F}[G(t)] = |f(\omega)|^2$ . Assuming that  $G(t)$  peaks at the origin, we expand  $G(t)$  near  $t = 0$ :  $G(t) = G_0 + \ddot{G}(0)t^2/2 + \dots$ , where we used  $\ddot{G}(0)$  to denote the second time derivative at the  $t = 0$  origin. Applying the Fourier transform to the expansion gives  $|f(\omega)|^2 = G_0\delta(\omega) - \pi\ddot{G}(0)\delta^{(2)}(\omega) + \dots$ . We use  $\delta(\omega)$  and  $\delta^{(2)}(\omega)$  to denote the Dirac delta function and its second derivative in the frequency domain, respectively. Now we insert the approximation in the signal fidelity calculation:

$$\int_{-\infty}^{\infty} r(\omega) |f(\omega)|^2 d\omega = \int_{-\infty}^{\infty} r(\omega) (G_0\delta(\omega) - \pi\ddot{G}(0)\delta^{(2)}(\omega) + \dots) = G_0r(0) - \pi\ddot{G}(0)r''(0) + \dots \quad (\text{C4})$$

In the above expression, we use  $r''(0)$  to denote the second derivative in the frequency space, as opposed to the derivative in time. The property of the derivative of delta functions can be proved by integration by parts. This gives us the final signal fidelity:

$$F_{\text{signal}} \approx \left| G_0r(0) - \pi\ddot{G}(0)r''(0) \right|^2. \quad (\text{C5})$$



As shown by the formula, the infidelity is given by the second derivative at the peak of the signal. Intuitively, we wish a flat input signal in the time domain so that  $\ddot{G}(0) \ll 1$  (longer pulse), and a broad window in the reflection spectrum ( $r''(0) \ll 1$ ) so that the signal can be minimally distorted.

We summarize the three different schemes in Table IV. Opting for a high fidelity protocol and a simple demonstration, we focus on the amplitude-based scheme in the main text. Nevertheless, to pursue a higher generation rate, future experiments may also adopt the phase-shift protocol, which requires a high quality, over-coupled spin-photon interface, careful design of the cavity detuning, and pulse shaping to minimize the waveform distortion.

#### Appendix D: Entanglement Fidelity of Microwave Retrieval

We characterize the microwave retrieval process by calculating its entanglement fidelity, which quantifies how well the microwave retrieval preserves the entanglement of the original spin-photon Bell state. For the initial Bell state,  $|\Phi\rangle = (|E\rangle_o |1\rangle_m + |L\rangle_o |0\rangle_m)/\sqrt{2}$ , where the subscripts  $o$  and  $m$  denote the optical photon and the microwave spin level, respectively, the dominant decoherence mechanisms are spin dephasing and transmon relaxation. We model these processes as a dephasing channel  $\mathcal{D}$  and an amplitude-damping channel  $\mathcal{L}$ , parameterized by the spin dephasing time  $T_{2,s}$  and the transmon relaxation time  $T_{1,t}$ , respectively. Defining the combined channel as  $\mathcal{E} = \mathcal{L} \circ \mathcal{D}$ , the entanglement fidelity is

$$\mathcal{F}_{\text{mw}} = \langle \Phi | (\mathbb{1}_o \otimes \mathcal{E}_m) (|\Phi\rangle \langle \Phi|) | \Phi \rangle. \quad (\text{D1})$$

The density matrix of  $|\Phi\rangle$  is

$$\rho = |\Phi\rangle \langle \Phi| = \frac{1}{2} (|E\rangle \langle E|_o |1\rangle \langle 1|_m + |E\rangle \langle L|_o |1\rangle \langle 0|_m + |L\rangle \langle E|_o |0\rangle \langle 1|_m + |L\rangle \langle L|_o |0\rangle \langle 0|_m). \quad (\text{D2})$$

Thus, the fidelity reduces to

$$\mathcal{F}_{\text{mw}} = \frac{1}{4} (\langle 1 | \mathcal{E}(|1\rangle \langle 1|) | 1 \rangle + \langle 1 | \mathcal{E}(|1\rangle \langle 0|) | 0 \rangle + \langle 0 | \mathcal{E}(|0\rangle \langle 1|) | 1 \rangle + \langle 0 | \mathcal{E}(|0\rangle \langle 0|) | 0 \rangle), \quad (\text{D3})$$

where the subscripts are dropped since only the microwave subsystem is affected by the channel.

For the qubit dephasing channel, the Kraus operators are  $M_{d,0} = \sqrt{1-p_d}I$ ,  $M_{d,1} = \begin{pmatrix} \sqrt{p_d} & 0 \\ 0 & 0 \end{pmatrix}$ , and  $M_{d,2} = \begin{pmatrix} 0 & 0 \\ 0 & \sqrt{p_d} \end{pmatrix}$ , where  $p_d$  is the dephasing probability. For the amplitude damping channel on the same basis, the Kraus operators are  $M_{a,0} = \begin{pmatrix} 1 & 0 \\ 0 & \sqrt{1-p_a} \end{pmatrix}$  and  $M_{a,1} = \begin{pmatrix} 0 & \sqrt{p_a} \\ 0 & 0 \end{pmatrix}$ , where  $p_a$  is the excited state decay probability. The action of the channel gives

$$\begin{aligned} \mathcal{E}(|0\rangle \langle 0|) &= |0\rangle \langle 0|, \\ \mathcal{E}(|0\rangle \langle 1|) &= \sqrt{1-p_a}(1-p_d)|0\rangle \langle 1|, \\ \mathcal{E}(|1\rangle \langle 0|) &= \sqrt{1-p_a}(1-p_d)|1\rangle \langle 0|, \\ \mathcal{E}(|1\rangle \langle 1|) &= p_a|0\rangle \langle 0| + (1-p_a)|1\rangle \langle 1|. \end{aligned}$$

Substituting these into the fidelity expression yields

$$\mathcal{F}_{\text{mw}} = \frac{1}{4} (1 + (1-p_a) + 2\sqrt{1-p_a}(1-p_d)). \quad (\text{D4})$$

The damping of the transmon excited state  $|e\rangle$  after  $\tau$  gives a  $p_a$  of  $1 - e^{-\tau/T_{1,t}}$ . One caveat is that the transmon is only excited after capturing the first microwave pulse, so the damping time is in fact  $\tau/2$ . However, due to the shelving, which put the transmon in the  $|f\rangle$  state, the decay is twice as fast. The two effects cancel, eventually gives  $p_a = 1 - e^{-\tau/T_{1,t}}$ . Spin dephasing during the entire retrieval window gives  $p_d = 1 - e^{-\tau/T_{2,s}}$ . Notice that the  $T_{2,s}$  is the  $T_2$  time of the spin without the presence of the resonator, where the decoherence process is dominated by the dephasing  $T_{1,s} \ll T_{2,s}$ . Substituting  $p_a$  and  $p_d$  yields the entanglement fidelity reported in the main text:

$$F_{\text{mw}} = \frac{1}{4} (1 + e^{-\tau/T_{1,t}} + 2e^{-\tau/2T_{1,t}}e^{-\tau/T_{2,s}}). \quad (\text{D5})$$

## Appendix E: Scheme Compatible Color Centers

In the main text, we demonstrate our scheme using the nitrogen-vacancy center and the tin-vacancy center. Our scheme can be generalized to other single defect centers provided that they satisfy the following requirements. For generating spin-photon entanglement, the system must demonstrate a robust spin initialization, well-resolved spin-dependent optical transitions, and microwave control over the spin levels. To realize our microwave readout scheme, the spin states must contain a qubit subspace and a gigahertz-range readout level that couples strongly to microwave. Moreover, the qubit subspace and the readout level must be connected with allowed transitions to enable microwave control.

Besides the demonstrated color defects in the main text, the neutrally charged silicon-vacancy ( $\text{SiV}^0$ ) center could also be a potential candidate [74, 75], although only ensemble spin resonance of  $\text{SiV}^0$  has been demonstrated [76]. The properties of the three color centers are compared in Table V. The  $\text{NV}^-$  and  $\text{SiV}^0$  have a spin-1 ground state  $m = \pm 1, 0$ . Two of the levels ( $\pm 1$ ) are degenerate in the zero-field limit. To establish a long-living qubit space, and strongly coupled readout level, the three levels need to be sufficiently split by a DC magnetic field. To create a mega-hertz level splitting between the  $\pm 1$  states, which makes the state decay negligible ( $< 10^{-3}$ ) during the readout, a small magnetic field (0.1 – 1 mT) is needed. The advantage of the spin-1 ground state is that it enables strong spin-microwave coupling, with magnetic dipole moment given by  $\gamma_e \langle 0 | \vec{S} | 1 \rangle = \gamma_e / \sqrt{2}$  [56]. The  $^{117}\text{SnV}^-$  ground state can be split by strain engineering and strong hyperfine interaction, as demonstrated in [52]. Therefore, it allows the operation of the scheme in zero-field. However, due to the hybridization of electron-nuclear spin in the ground state, the  $^{117}\text{SnV}^-$ 's dipole moment is only half of that of the  $\text{NV}^-$  and  $\text{SiV}^0$ . This is shown by a perturbation calculation in the Appendix E 1. The small magnetic dipole moment results in a low microwave retrieval efficiency. Moreover, due to the low transition frequency  $\sim 0.6$  GHz, the  $^{117}\text{SnV}^-$  faces higher thermal noise and potential frequency mismatch when coupled to a transmon qubit, which may be resolved by operating the scheme at a lower cryogenic temperature and employing a flux tunable superconducting qubit.

In terms of optical properties, the  $\text{NV}^-$  has a very small ( $\sim 0.03$ ) Debye-Waller factor (D-W factor), compared with a D-W factor of 0.9 for  $\text{SiV}^0$  and 0.6 for  $^{117}\text{SnV}^-$ . This results in  $\text{NV}^-$ 's small optical cooperativity, as shown in Appendix E 2. Nevertheless, given the high fineness of the optical cavity, and the large magnetic dipole moment, the  $\text{NV}^-$  still exceeds  $^{117}\text{SnV}^-$  in both fidelity and overall efficiency. If the small magnetic field is compatible with the experimental design, future research favors  $\text{NV}^-$  due to its high efficiency and fidelity in Bell pair generation. The  $^{117}\text{SnV}^-$  is favorable due to its zero-field protocol, and  $\text{SiV}^0$  is a powerful candidate that requires further investigation in its optical properties and single spin performance.

### 1. Perturbation Calculation of the Magnetic Dipole Moment of $^{117}\text{SnV}^-$

Following the analysis in [52], the unperturbed Hamiltonian contains strong spin-orbit and strain terms:

$$\hat{H}_0 = \frac{1}{2} \lambda \hat{\sigma}_z^L \hat{\sigma}_z^S - \frac{1}{2} (\alpha_{E_{gx}} \hat{\sigma}_x^L + \alpha_{E_{gy}} \hat{\sigma}_y^L). \quad (\text{E1})$$

The  $\lambda$  is the spin-orbit coupling strength around 830 GHz, and  $\alpha$  is the strain along  $x$  and  $y$  direction. We add superscript  $L$  and  $S$  to denote the spin-1/2 operator of the electron and the orbit. The hyperfine interaction is treated as the perturbation terms in the Hamiltonian:

$$\hat{H}' \approx \hat{H}_{HF} = \frac{1}{4} A_{\parallel} \hat{\sigma}_z^S \hat{\sigma}_z^I + \frac{1}{4} A_{\perp} (\hat{\sigma}_x^S \hat{\sigma}_x^I + \hat{\sigma}_y^S \hat{\sigma}_y^I), \quad (\text{E2})$$

where  $\hat{\sigma}^I$  is the spin-1/2 operator of the nuclear spin.  $A_{\parallel}$  and  $A_{\perp}$  are the parallel and perpendicular hyperfine interaction strength. We first diagonalize the unperturbed Hamiltonian to find the unperturbed eigenstates. We define the splitting  $\Delta = \sqrt{\lambda^2 + \alpha^2}$ , where  $\alpha = \sqrt{\alpha_{E_{gx}}^2 + \alpha_{E_{gy}}^2}$ . The unperturbed system has two degenerate energy levels,  $E^{(0)} = \pm \Delta/2$ .

For clarity, we can define  $c_1 = \sqrt{\frac{\Delta + \lambda}{2\Delta}}$ ,  $c_2 = \sqrt{\frac{\Delta - \lambda}{2\Delta}}$ ,  $e^{i\phi} = \frac{\alpha_{E_{gx}} + i\alpha_{E_{gy}}}{\alpha}$ . Then the four eigenstates can be written as

$$|\Psi_1\rangle = c_1 | +L, \uparrow S \rangle - c_2 e^{i\phi} | -L, \uparrow S \rangle \quad (\text{E3})$$

$$|\Psi_2\rangle = c_2 | +L, \downarrow S \rangle - c_1 e^{-i\phi} | -L, \downarrow S \rangle \quad (\text{E4})$$

	NV <sup>-</sup> [77]	SiV <sup>0</sup> [74]	Hyperfine <sup>117</sup> SnV <sup>-</sup> [52]
Radiative Lifetime ( $\tau_{\text{rad}}$ )	13 ns	2 ns	6 ns
Debye-Waller Factor ( $\xi$ )	0.03	0.9	0.6
ZPL Wavelength (nm)	637	946	620
Electric Dipole Moment	5.1 $D$	23.7 $D$	7.3 $D$
Optical Reflectivity	Yes	Unclear	Yes
DC Magnetic Field $\vec{B}$	0.1-1 mT	0.1-1 mT	0
Engineered Strain $\alpha$	0	May Require	900 GHz
MW qubit frequency (GHz)	2.9	1.0	0.6
Magnetic Dipole Moment	$\gamma_e/\sqrt{2}$	$\gamma_e/\sqrt{2}$	$\alpha\gamma_e/(2\sqrt{2}(\alpha^2 + \lambda^2))$

TABLE V. Comparison between different candidate color centers.  $\gamma_e$  is the gyromagnetic ratio of the electron. The magnetic dipole of the tin-vacancy center depends on the strain  $\alpha$  in the system, and the spin-orbit coupling  $\lambda$ . Here,  $D = 3.34 \times 10^{-30}$  C·m. Color center parameters are used for calculating the optical cooperativity and spin microwave coupling strength.

with energy  $E^{(0)} = +\Delta/2$ , and the other two

$$|\Psi_3\rangle = c_2 e^{-i\phi} |L, \uparrow S\rangle + c_1 |-L, \uparrow S\rangle \quad (\text{E5})$$

$$|\Psi_4\rangle = c_1 e^{i\phi} |L, \downarrow S\rangle + c_2 |-L, \downarrow S\rangle \quad (\text{E6})$$

with energy  $E^{(0)} = -\Delta/2$ . We denote the two orbital branches as  $\pm L$ , and the two electron spin states as  $\uparrow S$  and  $\downarrow S$ . To add in the hyperfine interaction, we use the degenerate perturbation by diagonalizing  $\hat{H}'$  within each degenerate manifold. We can look at the  $E^{(0)} = -\Delta/2$  manifold, which has a  $4 \times 4$  basis including nuclear spin:  $\{|\Psi_3, \uparrow\rangle, |\Psi_3, \downarrow\rangle, |\Psi_4, \uparrow\rangle, |\Psi_4, \downarrow\rangle\}$ .

We notice that the states with aligned electron and nuclear spin  $|\Psi_3, \uparrow\rangle$  and  $|\Psi_4, \downarrow\rangle$  are already eigenstates with energy  $\frac{A_{\parallel}}{4}$ . So, we just need to diagonalize within the subspace  $\{|\Psi_3, \downarrow\rangle, |\Psi_4, \uparrow\rangle\}$ . The Hamiltonian in this basis is

$$\hat{H}_{m_J=0} = \begin{pmatrix} -A_{\parallel}/4 & \frac{A_{\perp}\alpha}{2\Delta} \\ \frac{A_{\perp}\alpha}{2\Delta} & -A_{\parallel}/4 \end{pmatrix}, \quad (\text{E7})$$

where we assume that the strain is along one direction so that  $e^{i\phi} = 1$ , as implemented in [52]. The eigenvalues are the energy corrections  $E^{(1)}$ :  $E^{(1)} = -\frac{A_{\parallel}}{4} \pm \frac{A_{\perp}\alpha}{2\Delta}$ . The corresponding eigenstates, which correspond to the  $|0\rangle$  and  $|1\rangle$  state in the main text are

$$|E_{m_J=0'}^+\rangle = \frac{1}{\sqrt{2}}(|\Psi_3, \downarrow\rangle + |\Psi_4, \uparrow\rangle) \quad (\text{E8})$$

$$|E_{m_J=0''}^+\rangle = \frac{1}{\sqrt{2}}(|\Psi_3, \downarrow\rangle - |\Psi_4, \uparrow\rangle). \quad (\text{E9})$$

Now, we can evaluate the matrix element like  $\langle r | \vec{S} | 0 \rangle = \langle \Psi_3, \uparrow | \vec{S} | E_{m_J=0'}^+ \rangle$ . The orbitals do not contribute to the magnetic dipole moment. The electron spins contribute to strain-dependent magnetic dipole of  $\frac{1}{2\sqrt{2}} \frac{\gamma_e \alpha}{\Delta}$ . The nuclear spin has a contribution three orders of magnitude smaller than the electron spin. Given the strain  $\alpha = 928.4$  GHz in [52], the magnetic dipole of tin-vacancy is roughly 0.4 of the NV<sup>-</sup> magnetic dipole.

Our scheme may further be applied to molecular defects or other solid-state quantum emitters, which could have a stronger microwave coupling [21, 41, 56–58]; however, here we restrict the comparison to color centers.

## 2. Optical Cooperativity Estimation for NV<sup>-</sup>

Among the candidate color centers, the NV<sup>-</sup> has a small Debye-Waller factor 0.03, which means that the photon emission into the ZPL accounts for only a few percent of the total emission. To enhance the ZPL emission, we resonantly couple the NV<sup>-</sup>'s ZPL line to an optical cavity [78]. We assume the following model to find the effective cooperativity for the optical scheme.

The model consists of three levels with two ground states and one excited state labeled as  $|e\rangle$ ,  $|g_1\rangle$  and  $|g_2\rangle$  ( $\Lambda$ -configuration). The transition  $g_1$ - $e$  is the ZPL transition, and we model the emission into the phononic side-bands (PSB) as decay from  $|e\rangle$  to  $|g_2\rangle$ . The decay rate into two ground states is given by the branching ratio  $\gamma_1/\gamma_2 = \eta$ , and

$\gamma_1/(\gamma_1 + \gamma_2) = \gamma_1/\gamma = 0.03$  is the Debye-Waller factor of the NV. The ZPL transition is coupled to the cavity mode via the Jaynes-Cummings Hamiltonian. Given the tera-Hertz separation between the ZPL and the PSB, we ignore the coupling of the  $g_2$ - $e$  transition to the cavity.

Two of the Heisenberg-Langevin equations describing the spin-light dynamics are

$$\frac{d\hat{a}}{dt} = (-i\omega_c - \kappa)\hat{a} - ig\hat{\sigma}_{g_1e} + \sqrt{2\kappa_c}\hat{a}_{\text{in}}(t) \quad (\text{E10})$$

$$\frac{d\hat{\sigma}_{g_1e}}{dt} = (-i\omega_a - \frac{\gamma}{2})\hat{\sigma}_{g_1e} + ig\hat{\sigma}_z\hat{a} \quad (\text{E11})$$

where  $\hat{a}$  is the operator of the cavity mode,  $\hat{\sigma}_{g_1,e} = |g_1\rangle\langle e|$  is the operator of the  $g_1$ - $e$  transition, and  $\hat{\sigma}_z = |e\rangle\langle e| - |g_1\rangle\langle g_1|$ .  $\omega_c$  and  $\omega_a$  are the resonance frequencies of the cavity and the two-level atom respectively. The  $g$  is the ZPL-cavity coupling strength;  $\gamma$  is the total linewidth of  $\text{NV}^-$  in free space. The photon couples out from the cavity with rate  $\kappa_c$ . The cavity's internal loss rate is  $\kappa_i$ . The total cavity loss rate is  $\kappa = \kappa_i + \kappa_c$ . In the weak excitation limit (i.e. linear regime), the mean-field assumption applies  $\langle\hat{\sigma}_z\rangle = \langle\hat{a}\rangle\langle\sigma_z\rangle$ . We can obtain the reflectivity of the system using input-output relation:

$$\mathcal{R}(\omega) = \left| 1 - \frac{2\kappa_c}{i(\omega - \omega_c) + \kappa - \frac{g^2\langle\sigma_z\rangle}{i(\omega - \omega_a) + \gamma}} \right|^2. \quad (\text{E12})$$

$\langle\sigma_z\rangle = P_e - P_{g_1}$  is the population difference between the excited state and  $|g_1\rangle$ .

In the two-level system case, assuming that the system is weakly excited, we have  $\langle\sigma_z\rangle = P_e - P_{g_1} \approx -1$ , which recovers the reflectivity formula obtained in Eq. (C1). In the case of three-level system, although the excited state will not be populated  $P_e \approx 0$ , the population is split between the two ground states  $|g_1\rangle$  and  $|g_2\rangle$ , causing a smaller effective coupling. In free space, the initial excited state will decay into the two ground states according to the ratio  $\gamma_1/\gamma$  and  $\gamma_2/\gamma$ . Here, we calculate the ground state population in the presence of the cavity. We solve the Lindblad master equation of our system within the subspace spanned by  $\{|0, g_1\rangle, |0, g_2\rangle, |1, g_1\rangle, |0, e\rangle\}$ , where the number denotes the Fock states of the photon in the cavity. For convenience, let's label the states as  $\{|1\rangle, |2\rangle, |3\rangle, |4\rangle\}$  respectively. We assume that initially there is one photon in the cavity and the spin is polarized to the ground state  $|1, g_1\rangle = |3\rangle$ . Then, a closed set of coupled equations is:

$$\frac{d}{dt} \begin{pmatrix} \rho_{33} \\ \rho_{44} \\ \rho_{43} \\ \rho_{34} \end{pmatrix} = \begin{pmatrix} -\gamma & 0 & ig & -ig \\ 0 & -\kappa & -ig & ig \\ ig & -ig & -(\gamma + \kappa)/2 & 0 \\ -ig & ig & 0 & -(\gamma + \kappa)/2 \end{pmatrix} \begin{pmatrix} \rho_{33} \\ \rho_{44} \\ \rho_{43} \\ \rho_{34} \end{pmatrix}, \quad (\text{E13})$$

where we used the convention  $\rho_{34} = \langle 3|\rho|4\rangle$ , and the  $g_1$ - $e$  transition is resonant with the cavity. This set of equations describes the damped Rabi oscillation between the  $|3\rangle$  and  $|4\rangle$  states. The populations of the two ground states  $\rho_{11}$  and  $\rho_{22}$  are simply sourced by this dynamics.  $\frac{d\rho_{11}}{dt} = \kappa\rho_{44} + \gamma_1\rho_{33}$  and  $\frac{d\rho_{22}}{dt} = \gamma_2\rho_{33}$ . Solving the set of equations analytically gives the accumulation of population in the two ground states:

$$P_{g_1} = \rho_{11}(t = \infty) = \frac{\gamma\kappa(\gamma + \kappa) + 4g^2(\gamma_1 + \kappa)}{(\gamma + \kappa)(4g^2 + \gamma\kappa)}, \quad P_{g_2} = \rho_{22}(t = \infty) = \frac{4g^2\gamma_2}{(\gamma + \kappa)(4g^2 + \gamma\kappa)}. \quad (\text{E14})$$

In the case of  $\gamma \ll g \ll \kappa$ ,  $P_{g_1} \approx 1 - O(\gamma/\kappa)$  and  $P_{g_2} \approx 0 + O(\gamma/\kappa)$ . So,  $\langle\sigma_z\rangle \approx -1$ , and the coupling rate is not renormalized. Intuitively, the system dynamics is dominated by the cavity loss, so that the  $|g_2\rangle$  state remains mostly unpopulated. Therefore, the system behavior should remain similar to that of a driven two-level system with a total decay rate  $\gamma = \gamma_1 + \gamma_2$ . Given the above analysis, the cooperativity of the cavity-coupled  $\text{NV}^-$  system should be estimated to be  $C = g^2/(\kappa\gamma_{\text{tot}}) = g^2/(\kappa(\gamma_1 + \gamma_2))$ . In general, we should use the total spin linewidth for calculating the cooperativity  $C = g^2/(\kappa\gamma_{\text{tot}})$  and  $\gamma_{\text{tot}} = \gamma/\xi + \gamma^*$ , where  $\xi$  is the Debye-Waller factor and  $\gamma^*$  is the dephasing rate.

## Appendix F: Intrinsic Heralding Rate Estimation

In our protocol, the probability of heralding a successful entanglement event increases with the detection time which, however, also increases the runtime of each entanglement attempt. The total runtime of the experiment should be determined by the heralding rate, which takes into account both the detection time and success probability. In



TABLE VI. Intrinsic heralding rate for different colors using simulated parameters. We find the optimal detection time  $\tau_*$  for achieving the maximal heralding rate  $R_{\text{herald}}^*$ . The fidelity and probability at  $\tau_*$  are marked as  $\mathcal{F}_*$  and  $\mathcal{P}_*$ .

	$C$	$T_{\text{reset}}/\mu\text{s}$	$\Gamma/\text{kHz}$	$\tau_*/\mu\text{s}$	$R_{\text{herald}}^*$ (kHz)	$\mathcal{F}_*$	$\mathcal{P}_*$
$^{117}\text{SnV}^-$	43.1	10	$2\pi \times 0.9$	55	2.0	0.96	0.13
$\text{NV}^-$	12.8	10	$2\pi \times 3.9$	26	5.6	0.97	0.20
$\text{SiV}^0$	232.4	10	$2\pi \times 3.1$	29	5.5	0.99	0.21

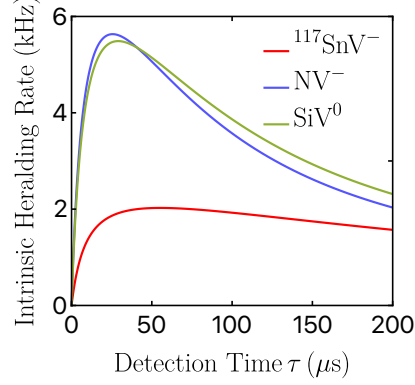


FIG. 6. Intrinsic Heralding Rate as a function of detection time  $\tau$  for different color centers using simulated parameters in Table VI.

this section, we consider only the intrinsic efficiency of the scheme, and ignore all external collection efficiency, e.g. the coupling efficiency of the optical fiber, transmission loss of the signal, and detector efficiency, etc.

The intrinsic heralding rate  $R_{\text{herald}}$  can be estimated as:  $R_{\text{herald}} = P_{\text{scheme}}/T_r$ , where  $P_{\text{scheme}}$  is the success probability of our scheme given by  $P_{\text{scheme}} = 0.5 \cdot \frac{C^2}{(1+C)^2} \cdot (1 - e^{-\Gamma\tau})$ , and  $T_r$  is the time taken for each round of attempted entanglement generation.  $T_r$  is mainly limited by the detection time  $\tau$  for each round, plus the reset and gate time  $T_{\text{reset}}$ . The intrinsic heralding rate, therefore, can be expressed as

$$R_{\text{herald}} = 0.5 \cdot \frac{C^2}{(1+C)^2} \cdot \frac{(1 - e^{-\Gamma\tau})}{\tau + T_{\text{reset}}}. \quad (\text{F1})$$

There exists an optimal detection time for the heralding rate. If the detection time is too long, the success probability of each round saturates to 1, and the rate decreases as  $1/\tau$ . If the detection time is smaller than the reset time  $\tau < T_{\text{reset}}$ , the rate decreases to zero as  $\tau/T_{\text{reset}}$ . In Fig. 6, we show the heralding rate as a function of the detection time. All the parameters we used for plotting are presented in Table VI, where the parameters  $C$  and  $\Gamma$  are given by the simulation, and we assume a constant  $T_{\text{reset}} = 10 \mu\text{s}$  that includes both the gate time and reset time. The optimal detection time  $\tau_*$  depends on the  $T_{\text{reset}}$  and  $\Gamma$ , and the numerical value of  $\tau_*$  is also shown in Table VI. The table also shows the fidelity and the success probability at the optimal detection time, which indicates that the best operational regime prefers fast and truncated microwave detection in each round, which ensures high fidelity of the heralded photon state while achieving the highest heralding rate.